

# Think Global, Act Local: The Influence of Environment Age and Host Mass on Type Ia Supernova Light Curves

B. M. ROSE,<sup>1</sup> P. M. GARNAVICH,<sup>1</sup> AND M. A. BERG<sup>1</sup>

<sup>1</sup>*University of Notre Dame, Center for Astrophysics, Notre Dame, IN 46556*

(Dated: February 6, 2019; Received November 12, 2018; Revised January 29, 2019; Accepted February 4, 2019)

Submitted to ApJ

## ABSTRACT

The reliability of Type Ia supernovae (SNIa) may be limited by the imprint of their galactic origins. To investigate the connection between supernovae and their host characteristics, we developed an improved method to estimate the stellar population age of the host as well as the local environment around the site of the supernova. We use a Bayesian method to estimate the star formation history and mass weighted age of a supernova’s environment by matching observed spectral energy distributions to a synthesized stellar population. Applying this age estimator to both the photometrically and spectroscopically classified Sloan Digital Sky Survey II supernovae (N=103) we find a  $0.114 \pm 0.039$  mag “step” in the average Hubble residual at a stellar age of  $\sim 8$  Gyr; it is nearly twice the size of the currently popular mass step. We then apply a principal component analysis on the SALT2 parameters, host stellar mass, and local environment age. We find that a new parameter, PC<sub>1</sub>, consisting of a linear combination of stretch, host stellar mass, and local age, shows a very significant ( $4.7\sigma$ ) correlation with Hubble residuals. There is a much broader range of PC<sub>1</sub> values found in the Hubble flow sample when compared with the Cepheid calibration galaxies. These samples have mildly statistically different average PC<sub>1</sub> values, at  $\sim 2.5\sigma$ , resulting in at most a 1.3% reduction in the evaluation of  $H_0$ . Despite accounting for the highly significant trend in SNIa Hubble residuals, there remains a 9% discrepancy between the most recent precision estimates of  $H_0$  using SNIa and the CMB.

**Keywords:** distance scale, galaxies: distances and redshifts, galaxies: general, galaxies: photometry, galaxies: stellar content, supernovae: general

## 1. INTRODUCTION

For decades, astronomers have been developing methods to better understand the variation in peak luminosities of Type Ia supernovae (SNIa) and improve their use as precision distance indicators. In 1993, Phillips identified a relationship between peak magnitude and the rate of fading in the light curves of SNIa. A connection between supernova color and peak luminosity was also shown to improve distance estimates of SNIa (Riess et al. 1996; Tripp & Branch 1999; Phillips et al. 1999). SNIa quickly became useful cosmological probes, measuring the expansion rate of the universe (Hamuy et al. 1995; Riess et al. 1995), the density of matter (Garnavich et al. 1998; Perlmutter et al. 1998), and the accelerated expan-

sion of the universe (Riess et al. 1998; Perlmutter et al. 1999).

The principle energy source that powers a SNIa light curve derives from the decay chain of <sup>56</sup>Ni that is synthesized in the runaway nuclear fusion at the start of the explosion (Arnett 1982). The radioactive nickel yield appears to vary by a factor of eight over the extreme range of typical SNIa luminosities. The mass of radioactive elements helps regulate the rate of recombination in iron group elements, and this results in the famous “Phillips relation” between the light curve decline rate and luminosity (Kasen & Woosley 2007).

The reason some SNIa synthesize nearly a solar mass of radioactive nickel while others are powered by a tenth of a solar mass remains uncertain. Models suggest that the speed of the fusion front moving through the white dwarf has a major influence on the radioactive yield. The transition between deflagration (subsonic fusion)

and detonation (supersonic fusion) may vary from supernova to supernova and this could explain the diversity in their luminosities. The variation in nickel yield appears to be influenced by host properties as Hamuy et al. (1996) and Hamuy et al. (2000) noted that low-luminosity SNIa tend to occur in passive galaxies like large ellipticals. This observation has been confirmed and expanded in several subsequent studies (Gallagher et al. 2005; Sullivan et al. 2006) which clearly demonstrate that host galaxies provide an important clue to the progenitors and explosion mechanisms of SNIa.

Metal abundance and population age are global properties of galaxies that could conceivably have an impact on a supernova’s  $^{56}\text{Ni}$  yield. Host properties that correlate with age or metallicity, such as galaxy mass, could also influence the character of a supernova explosion. For example, Timmes et al. (2003) proposed that the metal abundance during the main sequence stage could affect the neutron fraction in the resulting white dwarf stars. They predicted that high metal abundance populations will generate low radioactive yields and, thus, faint supernovae. Applying the galactic mass-metallicity relationship to this finding, SNIa from large galaxies would then be systematically fainter just as was seen in Hamuy et al. (2000). Bravo et al. (2010) derived a similar luminosity-metallicity relationship, but 3D calculations by Röpke & Hillebrandt (2004) suggest the effect is much smaller than originally envisioned. An observational test of this hypothesis by Gallagher et al. (2008) looked at SNIa in elliptical galaxies and found trends with both age and metallicity, although this was disputed by Howell et al. (2009).

A sensitive test of the environmental effects on SNIa is to study the scatter in a SNIa Hubble diagram after light curve shape and color corrections have been applied. This type of analysis is also important for constraining systematic errors in cosmological measurements. Hubble residuals are the difference between the luminosity distance and the expected distance from the best fit cosmology and are most powerful in the “Hubble flow” where peculiar velocities are small compared with the expansion velocity. Woosley et al. (2007) and Kasen et al. (2009) showed that explosion asymmetries, metallicity variations, kinetic energy variations, and other explosion parameters can produce a dispersion in the Phillips relation for a fixed radioactive yield. These relationships present the possibility of using Hubble residuals to probe supernova physics. Research over the past several years indicates that some host galaxy properties correlate with Hubble residuals (e.g. Sullivan et al. 2010; Lampeitl et al. 2010; Childress et al. 2013).

Surprisingly, the strongest correlation between Hubble residuals and galaxy properties appears to be with the host stellar mass. The effect is called the “mass step” because at  $\sim 10^{10} M_{\odot}$  there appears to be a jump in the average Hubble residual. This led to extensive work on understanding the physical properties such as population age and metallicity that could underlie the mass correlation (e.g. Gupta et al. 2011; Hayden et al. 2013; Moreno-Raya et al. 2016a,b). Childress et al. (2014) has proposed that the mass correlation is really an age effect amplified by galaxy “downsizing.” This research has been fruitful, but not definitive. Ongoing analyses of SNIa data sets continue to debate the significance of these effects (e.g. Graur et al. 2016; Jones et al. 2018, for LOSS and Foundation respectively).

Rigault et al. (2013) and Rigault et al. (2018) looked at star formation and specific star formation rates respectively at the sites of SNIa explosions by measuring  $H_{\alpha}$  emission strength using spatially resolved spectroscopy. They found a very significant step in corrected SNIa peak luminosity as a function of the specific star formation rate at the location of the explosion. This research identified a set of SNIa with a 0.2 mag offset in Hubble residual that are generally found in regions of lower star formation rate. There is still not a consensus on the impact of local star formation rates on Hubble residual especially when these trends are measured using UV observations (Rigault et al. 2015; Jones et al. 2015).

A very recent study (Jones et al. 2018) on a large low-redshift data set (the Foundation sample, Foley et al. 2017) compared Hubble residual with host galaxy stellar mass, local environment mass (the region within a radius of 1.5 kpc of the SNIa), host galaxy rest frame  $u - g$  color, and local environment rest frame  $u - g$  color. The rest frame  $u - g$  color is a simple way to estimate recent star formation, and therefore, a crude age estimator. They found that the local environment contained no new information compared to the global parameters.

In addition, there appears to be a tension between the  $H_0$  estimated from the cosmic microwave background observations (Planck Collaboration 2016; Planck Collaboration et al. 2018) and estimates based on SNIa. These precision measurements now disagree by  $3.8\sigma$  (Riess et al. 2016, 2018) due to either new physics or a systematic bias in one of the measurements. The SNIa host environment is of particular importance to the precision measurements of the Hubble constant ( $H_0$ ). The Cepheid variables used to calibrate the SNIa peak absolute magnitude are massive stars, so are observed only in star-forming galaxies. In contrast, supernovae discovered in unbiased searches are found in all types of

galaxies. A mass step correction between the Cepheid calibrated hosts and the Hubble flow galaxies is currently applied to the data (at  $\pm 0.03$  mag) and provides a relatively minor tweak to the value of  $H_0$  derived from supernovae. So, at present, host environment is not a major contributor to the uncertainty budgets of cosmological measurements.

Here, we scrutinize the relation between Hubble residual and the age of the stellar population derived from host galaxy colors. We develop a technique to translate multi-band galaxy photometry into an estimate of the star formation history and finally an average age for the stellar population. In principle, colors should be a better indicator of SNIa progenitor age than  $H_\alpha$ . This is because after a single burst of star formation,  $H_\alpha$  emitting HII regions are dissipating just as SNIa are beginning to explode. We apply our technique to both the global photometry of SNIa host galaxies and to the specific populations at the sites of the explosions. We then compare the local and global ages with SNIa characteristics, and other host properties to determine the parameters that have the largest impact on the measured Hubble residual. Finally, we investigate how our estimated ages may influence the current SNIa measurements of  $H_0$  and its error budget.

## 2. DATA

For our primary analysis, we use SNIa that were discovered with the SDSS-II Supernova survey (Sako et al. 2008). We selected both spectroscopic and photometric classified SNIa that passed cosmology cuts as described and released by Campbell et al. (2013). This cosmological data set, including their SALT2 (Guy et al. 2007, 2010) calibration parameters, are available online. Hereafter we will refer to Campbell et al. (2013) as C13. For our analysis, a few additional cuts were applied. For quality, we limited our analysis to objects whose photometric uncertainty is less than 1.5 mag. These cuts are dominated by low quality  $u$ -band magnitudes. In the end, the resulting  $g$ - and  $i$ -band maximum uncertainties are less than 0.3 mag, and less than 0.16 mag for  $r$ -band. In addition we removed objects that had a Hubble residual greater than 0.7 mag. Looking at Figure 16 of C13, these objects are likely core collapse supernovae that passed the color-magnitude cut.

This data set does not use the most recent standardization tools, such as BEAMS with Bias Corrections applied to the Pantheon data set (Kessler & Scolnic 2017; Scolnic et al. 2018). Restricting ourselves to SDSS photometry and low-redshift events avoids several of the biases mitigated in the Pantheon analysis while still providing a large, uniform sample.

The software developed for the data aggregation and analysis described in this paper is available at <https://github.com/benjaminrose/mc-age>.

### 2.1. Local Environment Photometry

The photometry of the environment around the site of the supernovae are taken from the “Scene Modeling” method described in Holtzman et al. (2008). The method incorporates all the images taken during the survey to build a photometric model at the location of the transient. The resulting photometry at the site is a convolution of the galaxy on the scale of the typical seeing. By applying this fixed angular aperture we always get the most compact local environment possible. Finally, in order to keep the environment truly “local,” a redshift cutoff was imposed,  $z < 0.2$ . With the average seeing for SDSS being  $1.4''$ , the maximum extent of a galaxy’s local environment was 3 kpc in radius. At higher redshifts the angular resolution encompasses a majority of typical galaxy and there is little difference between local and global properties. The typical size of the projected aperture defining the environment at the supernova location was 1.5 kpc.

Since core collapse supernovae are less luminous than SNIa, their contamination percentage increases in the low redshift portion of any data set. Anticipating this higher percentage of core collapse supernova (CC) interlopers, we added further Hubble residual cut to minimize the CC contamination. In addition, the statistics used in this work are robust against the  $\gtrsim 3.9\%$  CC contamination estimated in C13. A detailed study of CC contamination affecting SNIa standardization with host galaxy properties should be done since the ratio of SNIa and CC is highly dependent on host properties.

This results in a final data set of 103 SNIa. A partial list of the final data set used in the local environment analysis is visible in Table 1.

### 2.2. Global Photometry

In addition to the photometry of the local environment, we also study the correlation between the supernova characteristics and the host properties as a whole (hereafter the global properties). From the global host properties we can compare our results directly to the work presented in Gupta et al. (2011), hereafter G11, to check if our age estimator is more sensitive to younger stellar populations. Secondly, we can contrast the local and global properties of hosts to check if there is more information contained in the local environment rather than the more easily studied global properties.

The final analysis of G11 included 206 SNIa and hosts. We looked at the 76 objects that passed our redshift and

**Table 1.** Local environment data for [Campbell et al. \(2013\)](#) SNIa

SDSS ID	redshift	uncert. $\times 10^{-5}$	u [mag]	g [mag]	r [mag]	i [mag]	z [mag]	$\sigma_u$ [mag]	$\sigma_g$ [mag]	$\sigma_r$ [mag]	$\sigma_i$ [mag]	$\sigma_z$ [mag]	HR [mag]	uncert. [mag]
762	0.19138	2.4	24.65	23.82	22.95	22.61	22.18	0.79	0.09	0.04	0.04	0.13	0.15	0.08
1032	0.12975	3.3	24.92	24.74	23.73	23.32	22.87	0.61	0.16	0.09	0.11	0.26	-0.15	0.12
1371	0.11934	2.6	23.22	21.52	20.42	20.00	19.62	0.16	0.01	0.00	0.006	0.01	-0.13	0.06
1794	0.14191	6.3	23.76	23.77	23.09	22.89	22.81	0.43	0.11	0.08	0.06	0.24	0.27	0.08
2372	0.18046	2.2	24.81	22.85	21.84	21.40	21.02	0.87	0.03	0.01	0.01	0.03	-0.12	0.06

NOTE—Full machine readable data set is [available in the online journal](#).

**Table 2.** Data used for validation with [Gupta et al. \(2011\)](#) ages

SDSS ID	redshift	u [mag]	g [mag]	r [mag]	i [mag]	z [mag]	$\sigma_u$ [mag]	$\sigma_g$ [mag]	$\sigma_r$ [mag]	$\sigma_i$ [mag]	$\sigma_z$ [mag]
1166	0.3820	22.54	21.83	20.04	19.38	19.03	0.48	0.11	0.04	0.03	0.08
1580	0.1830	24.99	20.41	19.21	18.72	18.28	1.35	0.03	0.02	0.02	0.04
2165	0.2880	22.82	23.35	22.04	22.22	21.28	0.38	0.24	0.12	0.20	0.36
2422	0.2650	23.64	22.86	22.00	21.95	22.01	0.90	0.23	0.17	0.24	0.76
2789	0.2905	22.01	20.92	19.42	18.84	18.39	0.35	0.05	0.02	0.02	0.06

NOTE—Full machine readable data set is [available in the online journal](#).

other quality cuts to use in our method validation. A sample of the data set used for this validation is visible in Table 2.

For each of the 103 hosts where we had local environment photometry, we gathered the SDSS-DR12 model magnitudes for the estimate of the global properties. A sample of this data set can be seen in Table 3.

### 2.3. Photometry of Nearby Galaxies

The SDSS model magnitudes are unreliable for galaxies with a large angular extent. For the nearby galaxies with distances calibrated with Cepheid variable stars, we used aperture photometry to obtain both the local and global magnitudes. Images of the large galaxies were downloaded from the SDSS DR12 and individual apertures were designed to capture 90% of the combined light in all the filters. After masking out stars projected on the galaxy, the aperture was then applied to the image of each filter. The magnitude was then calibrated using nearby stars. The photometry for these galaxies can be seen in Table 4.

### 2.4. Supernova Properties

We use the [C13](#) supernova sample to provide light curve properties and Hubble residual information. We

use the Malmquist bias corrected distances derived from the best fit cosmology ( $H_0 = 73.8 \text{ km s}^{-1} \text{ Mpc}^{-1}$ ,  $\Omega_M = 0.24$ , and  $\Omega_\Lambda = 0.76$ ). When needed, we use these values for our assumed cosmology. For the maximum redshift in our sample, the Malmquist bias correction is  $\sim 0.01 \text{ mag}$ . However, [C13](#) noted that the stretch correction coefficient,  $\alpha$  they found for their full sample was significantly larger than typical and larger than the  $\alpha$  derived from their spectroscopically classified sub-sample. After our cuts, we found a significant correlation between the supernova stretch parameters,  $x_1$ , and the [C13](#) Hubble residuals which would likely result in spurious correlations with our host galaxy analysis. We corrected the [C13](#) Hubble residuals using their spectroscopically derived  $\alpha$  value of 0.16 and no longer detected a significant correlation between  $x_1$  and our sample’s Hubble residuals. The resulting Hubble residuals can also be found in Table 1.

For the nearby SNIa used in the Cepheid calibration of SNIa peak luminosity, we obtained light curves from the SNANA database<sup>1</sup> and fit them using SALT2.4 imple-

<sup>1</sup> <http://snana.uchicago.edu>

**Table 3.** Global host data for [Campbell et al. \(2013\)](#) SNIa

SDSS ID	u	g	r	i	z	$\sigma_u$	$\sigma_g$	$\sigma_r$	$\sigma_i$	$\sigma_z$
	[mag]	[mag]	[mag]	[mag]	[mag]	[mag]	[mag]	[mag]	[mag]	[mag]
762	20.34	18.50	17.46	17.01	16.70	0.13	0.01	0.01	0.01	0.02
1032	21.49	19.40	18.30	17.83	17.47	0.19	0.01	0.01	0.01	0.02
1371	20.60	18.62	17.55	17.10	16.68	0.08	0.01	0.01	0.01	0.01
1794	22.37	20.76	20.37	20.10	20.12	0.45	0.05	0.06	0.08	0.29
2372	21.79	20.50	19.53	19.02	18.59	0.24	0.03	0.02	0.02	0.05

NOTE—Full machine readable data set is [available in the online journal](#).**Table 4.** SEDs and redshifts for nearby galaxies

Host Galaxy	SNIa	redshift	Local SED					Global SED				
			u	g	r	i	z	u	g	r	i	z
M101	2011fe	0.000804	14.73	13.28	12.87	12.65	12.71	11.63	10.14	9.56	9.24	9.02
NGC 1015	2009ig	0.008797	14.54	12.93	12.19	11.78	11.53	18.49	16.91	16.19	15.74	15.54
NGC 1309	2002fk	0.007138	15.10	13.96	13.46	13.18	13.01	12.93	11.97	11.54	11.33	11.19
NGC 3021	1995al	0.00535	15.24	14.05	13.44	13.12	12.86	13.76	12.61	12.02	11.71	11.44
NGC 3370	1994ae	0.004276	17.08	15.97	15.50	15.23	15.06	13.63	12.58	12.06	11.79	11.56
NGC 3447	2012ht	0.003556	17.53	16.33	15.88	15.65	15.55	14.78	13.82	13.41	13.23	13.07
NGC 3972	2011by	0.002799	16.85	15.69	15.09	14.71	14.60	14.07	12.86	12.24	11.88	11.66
NGC 3982	1998aq	0.00371	15.28	14.16	13.72	13.43	13.27	12.95	11.92	11.45	11.17	10.98
NGC 4424	2012cg	0.00162	13.93	12.90	12.35	11.88	11.85	12.97	11.87	11.28	10.78	10.77
NGC 4536	1981B	0.00603	16.51	15.30	14.77	14.50	14.43	12.60	11.32	10.64	10.28	10.03
NGC 4639	1990N	0.00364	18.04	16.91	16.46	16.14	16.12	13.40	12.11	11.46	11.12	10.89
NGC 5584	2007af	0.005525	17.01	15.94	15.47	15.16	15.26	13.39	12.41	11.92	11.59	11.64
NGC 7250	2013dy	0.0039	15.35	14.63	14.17	14.08	13.88	14.27	13.48	13.04	12.93	12.72
UGC 9391	2003du	0.00649	17.80	16.79	16.39	16.21	16.06	16.05	15.15	14.78	14.62	14.42

NOTE—The uncertainties in the photometry are  $\pm 0.03$ .

mented from the `sncosmo`<sup>2</sup>. The model also corrected for Milky Way dust extinction from the dust maps of [Schlegel et al. \(1998\)](#) and [Schlafly & Finkbeiner \(2011\)](#) via `sfdmap`<sup>3</sup>.

### 3. STELLAR POPULATION MODEL

A direct estimate of the age of the stellar population requires a robust model for the observed population. Flexible Stellar Population Synthesis (FSPS) ([Conroy et al. 2009](#); [Conroy & Gunn 2010](#)) takes a star formation history and outputs either a spectrum or a redshifted spectral energy distribution (SED) of the resulting stel-

lar population. The version of FSPS we used (commit `ae31b2f` from November 2016) uses the MIST isochrones ([Dotter 2016](#); [Choi et al. 2016](#)) and the MILES spectral libraries ([Falc3n-Barroso et al. 2011](#)).

#### 3.1. FSPS settings

Many of the FSPS parameters were set at their default values, but a number of key settings were adjusted to produce the desired model space.

To control the metallicity of our stellar population, we set `zcontinuous` = 2. This setting convolves the SSPs (simple stellar populations) with a metallicity distribution function. The metallicity distribution is defined as

$$(Ze^{-Z})^{\text{pmetals}} \quad (1)$$

<sup>2</sup> <https://sncosmo.readthedocs.io/>

<sup>3</sup> <https://github.com/kbarbary/sfdmap>



with

$$Z \equiv \frac{z}{z_{\odot} 10^{\log(z/z_{\odot})}} \quad (2)$$

where  $z$  is the metallicity in linear units and  $z_{\odot} = 0.019$ . This metallicity distribution is governed by two more FSPS parameters: `pmetals` and `logzsol` (i.e.  $\log(z/z_{\odot})$ ). We left `pmetals` at its default value of 2 and during the fitting process `logzsol` was allowed to vary but was marginalized over when the age probability distribution was determined.

The next set of parameters govern the treatment of dust. We used the default power law dust model as explained in [Conroy et al. \(2009\)](#), based off of [Charlot & Fall \(2000\)](#). The attenuation curve of a star, as a function of stellar age, is defined as

$$\tau_{\lambda}(t) = \begin{cases} \tau_1(\lambda/5500 \text{ \AA})^{-0.7} & t \leq 10^7 \text{ yr} \\ \tau_2(\lambda/5500 \text{ \AA})^{-0.7} & t > 10^7 \text{ yr} \end{cases} \quad (3)$$

where  $\tau_1$  and  $\tau_2$  are the attenuation around a young stellar population and in the ISM respectively. See [Charlot & Fall \(2000\)](#) Figure 1 for a visual representation. In FSPS these two parameters are controlled via the `dust1` and `dust2` variables. For this analysis, `dust1` was set to two times `dust2`, and `dust2` was allowed to vary to match the observations. [Conroy et al. \(2009\)](#) claims good values of `dust1` and `dust2` are 1.0 and 0.3 respectively, while [Charlot & Fall \(2000\)](#) prefers values of `dust1` and `dust2` of 1.0 and 0.5 respectively. The allowed range for `dust2` in this analysis is explained in Section 4.2 and is consistent with these recommendations.

A few of the host SEDs show an unusual, e.g. SN4019. Adding nebular emission (setting `add_neb_emission` = `True` and `cloudy_dust` = `True`) adjusts the  $r$ -band magnitude for a young stellar population and allows the model to match this observed feature. This characteristic is shown to be achievable in the self-consistency validation test number 3, as explained in Section 5.1.

Finally, FSPS outputs the luminosity of  $1 M_{\odot}$ , so an extra constant,  $\delta$ , is used to scale the output SED of FSPS to match the observed SEDs.

### 3.2. Star Formation History

FSPS has many inputs for describing the star formation history of a galaxy. The `sfh` parameter allows the user to select the functional form of star formation history. [G11](#) used the simple  $\tau$ -model: the star formation rate is proportional to  $e^{-t/\tau}$ , with  $t$  being the time since the start of star formation and  $\tau$  is a free parameter. [G11](#) fit both  $\tau$  and the length of star formation history. This is the simplest model, which is important when fitting a small number of free parameters. However, such

a simple prescription makes it difficult to create a model with both old stars and recent star formation.

[Simha et al. \(2014\)](#) investigated the ability of several star formation history models to match simulated galaxies. This research looked at the simple  $\tau$ -model, a linear-exponent model<sup>4</sup>, and a four parameter  $\tau$ -model. A visual comparison is presented in Figures 3–5 of [Simha et al.](#). According to the calculations in [Simha et al.](#), the simple  $\tau$ -model can overestimate the age by  $\sim 1$ –2 Gyr, particularly for younger populations. Since we expect some supernovae to explode in young ( $\lesssim 2$  Gyr) stellar populations, we decided to use a four parameter  $\tau$ -model.

The main feature of the four-parameter  $\tau$ -model (4p $\tau$ -model) is that it separates the properties of early and late time star formation. This model can describe a wide range of star formation histories: an early burst, a history dominated by recent star formation, or both an early burst and recent star formation. The 4p $\tau$ -model is a piecewise combination of a linear-exponent star formation history then a linearly rising or falling star formation. This model is used by FSPS when `sfh` = 5. Mathematically the 4p $\tau$ -model can be written as

$$\Psi_{\star}(t) \propto \begin{cases} (t - t_0) e^{-(t-t_0)/\tau} & t_0 \leq t \leq t_i \\ \Psi_{\star}(t_i) + m_{\text{sf}} \mathcal{R}(t - t_i) & t_i < t \leq \mathcal{A}(z) \\ 0 & \text{else} \end{cases} \quad (4)$$

where  $t_0$  is when the star formation started,  $\tau$  is the e-folding parameter,  $t_i$  is the star formation transition time,  $m_{\text{sf}}$  is the slope of the late time star formation,  $\mathcal{R}$  is the ramp function, and  $\mathcal{A}(z)$  is the redshift dependant time when the observed light was emitted. Note that the equation above allows negative values of  $\Psi$ , which is nonphysical. So we add an extra constraint that forces  $\Psi(t)$  to be 0 if calculated to be negative. The four variables in the equation ( $t_0$ ,  $\tau$ ,  $t_i$ ,  $m_{\text{sf}}$ ) are the free parameters that give this model its name. These correspond to the FSPS parameters `sf_start`, `tau`, `sf_trunc`, and `sf_slope` respectively. Also, this function takes  $t$  as the time from the start of the universe. A sample of various star formation histories calculated from the tau model can be seen in Figure 1.

### 3.3. Calculating Ages

For any set of star formation parameters we determine the average population age. The mass weighted average

<sup>4</sup> This is the same as FSPS's delayed  $\tau$ -model, `sfh` = 4.

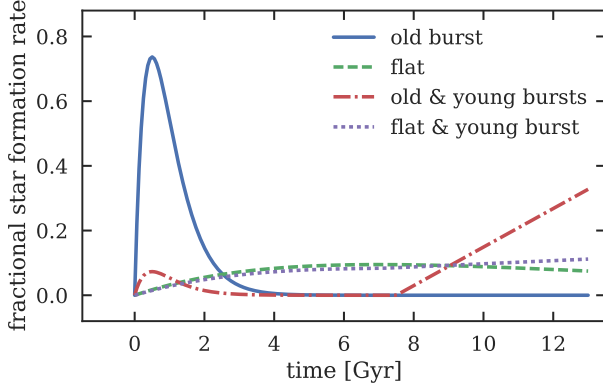


**Figure 1.** An example of several four-parameter  $\tau$ -model star formation histories. These star formation histories are normalized to produce the same total stellar mass. The old bursts have a  $\tau = 0.5$  and “flat” histories have a  $\tau = 7.0$ . The two examples of young bursts show how the number of young stars produced after  $t = t_i$  depends heavily on the amount of previously formed stars even for the same  $m_{\text{sf}}$ .

age is:

$$\langle A \rangle_{\text{mass}} = \mathcal{A}(z) - t_0 - \frac{\int_{t_0}^{\mathcal{A}(z)} (t - t_0) \Psi_{\star}(t) dt}{\int_{t_0}^{\mathcal{A}(z)} \Psi_{\star}(t) dt} \quad (5)$$

where all of the variables are the same as described in Equation (4) so  $t - t_0$  is simply the length of star formation. In the integral, a variable substitution of  $t - t_0 \rightarrow t$  transforms the time zero point from the beginning of the universe to the start of star formation. We would also need to transform  $\Psi_{\star}(t) \rightarrow \Psi'_{\star}(t)$  so that  $\Psi'_{\star}$  assumes  $t = 0$  is the start of star formation. This makes the equation for the mass weighted average age to be

$$\langle A \rangle_{\text{mass}} = \mathcal{A}(z) - t_0 - \frac{\int_0^{\mathcal{A}(z)-t_0} t \Psi'_{\star}(t) dt}{\int_0^{\mathcal{A}(z)-t_0} \Psi'_{\star}(t) dt}$$

or the equation used in G11. In this paper, the age of a stellar population will refer to the mass weighted average described here.

The model using the star formation parameters  $t_0 = 8.0$ ,  $\tau = 0.1$ ,  $t_i = 12$ , and  $m_{\text{sf}} = 20$ , produces a population with an average age of 437 Myr. This demonstrates that our SFH prescription can generate a dominant young population when SNIa are expected to start exploding. A small  $\tau$  is needed to keep the number of old stars from building up over the cosmic time and dominating over the recent linear star formation period. An example of this can be seen by the “old & young burst” star formation history in Figure 1.

#### 4. DETERMINING THE MOST PROBABLE SFH

Using Bayesian statistics and a Markov chain Monte Carlo (MCMC) sampling method we determine the

probability of each free parameter described in Section 3:  $\log(z/z_{\odot})$ ,  $\tau_2$ ,  $\tau$ ,  $t_0$ ,  $t_i$ ,  $m_{\text{sf}}$ , and  $\delta$ . Data modeling and parameter estimation is often done with Bayesian statistics because it calculates the probability of the model parameters given the observed data by using Bayes’ Theorem:

$$P(\theta|D) = \frac{P(D|\theta)P(\theta)}{P(D)} \quad (6)$$

where  $\theta$  is a given model’s parameters and  $D$  represents the observed data. Each probability is:

$P(\theta|D)$ : The *posterior*, which is the probability of the model parameters given the data.

$P(D|\theta)$ : The standard *likelihood* function,  $\mathcal{L}(D|\theta)$ .

$P(\theta)$ : The model *prior*, which describes what we know about the model before considering the data  $D$ , such as model parameter limits.

$P(D)$ : The model *evidence*, which in practice amounts to a normalization term.

For MCMC sampling, only relative probabilities are needed, so  $P(D)$  is generally ignored and Equation (6) becomes a proportionality, not an equality. It is common to use flat priors,  $P(\theta) \propto 1$ . In this case Bayes’ Theorem simplifies to a standard frequentist likelihood estimation,  $P(\theta|D) \propto \mathcal{L}(D|F)$ . More generally, some prior information is used and Bayes’ Theorem becomes

$$P(\theta|D) \propto P(\theta) \times \mathcal{L}(D|\theta). \quad (7)$$

To find the maximum posterior probability of the model parameters, we need only to know the priors,  $P(\theta)$ , and the likelihood of the data,  $\mathcal{L}(D|\theta)$ . A more complete description of Bayesian statistics and MCMC sampling is available in VanderPlas (2014) and Hogg & Foreman-Mackey (2017).

##### 4.1. Likelihood

This method uses a standard log-likelihood function for data with Gaussian uncertainties. Summing over each filter, we compare the observed apparent magnitude ( $m_i$ ) with the resulting apparent magnitude from FSPS ( $m_{\text{FSPS},i}$ ) plus a scaling factor ( $\delta$ ) to account for FSPS’s  $1 M_{\odot}$  output. Mathematically this is written as:

$$\ln(\mathcal{L}) \propto \sum_i \frac{(m_i - (m_{\text{FSPS},i} + \delta))^2}{\sigma_i^2} + \ln(2\pi\sigma_i^2) \quad (8)$$

with  $\sigma_i$  as the uncertainty in each  $m_i$  measurement.

#### 4.2. Priors

For five of the variables we use bounded flat tops as described below:

$$\begin{aligned}
 2.5 < t_i < \mathcal{A}(z) \\
 0.1 < \tau < 10 \\
 -1.520838 < \phi < 1.520838 \\
 0.5 < t_0 < t_i - 2.0 \\
 -45.0 < \delta < -5.0
 \end{aligned} \tag{9}$$

Since a flat distribution in a slope parameter preferentially searches the high values space,<sup>5</sup> the MCMC was performed over  $\phi$ , the angle the ramp function makes with respect to the  $x$ -axis; therefore,  $m_{\text{sf}} = \arctan(\phi)$ . The prior bound above,  $-1.520838 < \phi < 1.520838$ , corresponds to  $-20 < m_{\text{sf}} < 20$ .

In addition,  $\log(z/z_{\odot})$  uses a Gaussian distribution with  $\mu = -0.5$  dex and  $\sigma = 0.5$  dex limited to the range of  $-2.5 < \log(z/z_{\odot}) < 0.5$ . This is a common assumption as seen in [Belczynski et al. \(2016\)](#). Our model reaches a lower metallicity than the grid search used in [G11](#).

For the ISM dust parameter,  $\tau_2$ , we assume a Gaussian prior on the top bounds. The Gaussian distribution is defined by  $\mu = 0.3$  and  $\sigma = 0.2$ , but only values between 0 and 0.9 are accepted. This allows for some variability but keeps the values near the 0.3 and 0.5 as recommended by [Conroy et al. \(2009\)](#) and [Charlot & Fall \(2000\)](#) respectively.

### 5. VALIDATION

Following the statistical method described in Section 4, we derive probability distributions for the model parameters defined in Section 3. Using Equation (5) at each step in the MCMC chain, we build a probability distribution function for the age marginalized over metallicity and host galaxy dust.

#### 5.1. Self-consistency

The first validation of this newly developed age estimator was to verify that it was self-consistent, i.e. it could correctly estimate the star formation parameters from an SED generated by FSPS.

Eight different models were used in this test. The initial metallicity, dust, and star formation parameters can be seen in Table 5. These values were put into FSPS, at a redshift of  $z = 0.05$ , to generate observed SEDs. The resulting SEDs, Table 6, were then analyzed with

**Table 5.** SFH parameters used in the self consistency test

ID	$\log(z/z_{\odot})$	$\tau_2$	$\tau$ [Gyr <sup>-1</sup> ]	$t_0$ [Gyr]	$t_i$ [Gyr]	$\phi$ [rad]	age [Gyr]
1	-0.5	0.1	0.5	1.5	9.0	-0.785	10.68
2	-0.5	0.1	0.5	1.5	9.0	1.504	1.41
3	-0.5	0.1	7.0	3.0	10.0	1.504	1.75
4	-0.5	0.1	7.0	3.0	13.0	0.0	4.28
5	-1.5	0.1	0.5	1.5	9.0	-0.785	10.68
6	-0.5	0.8	7.0	3.0	10.0	1.504	1.75
7	-0.5	0.1	0.5	1.5	6.0	1.504	2.40
8	-0.5	0.1	0.1	8.0	12.0	1.52	0.437

NOTE—All models are at a  $z = 0.05$ .

**Table 6.** SEDs for the self consistency test

ID	u [mag]	g [mag]	r [mag]	i [mag]	z [mag]	$\langle A \rangle$ [Gyr]
1	20.36	18.76	17.99	17.67	17.39	$8.5 \pm 1.5$
2	20.31	18.74	17.98	17.66	17.39	$7.7 \pm 1.5$
3	16.15	15.43	15.40	15.19	15.21	$1.4 \pm 0.5$
4	17.65	16.74	16.49	16.26	16.16	$4.2 \pm 1.0$
5	19.69	18.29	17.70	17.45	17.29	$7.2 \pm 1.6$
6	17.66	16.58	16.25	16.01	15.86	$2.7 \pm 0.8$
7	17.62	16.80	16.57	16.34	16.26	$4.5 \pm 1.4$
8	19.72	18.37	17.88	17.68	17.56	$4.4 \pm 1.1$

NOTE—SEDs were scaled with a  $\delta = -25$  mag.

our Bayesian estimator. This set of models produced old populations ( $\sim 10.5$  Gyr) and very young populations ( $\sim 0.5$  Gyr). They explored the effect of metallicity (Model 5) and dust (Model 6). Model 2 also looked at a “mixed” population with an old burst of star formation and a strong increase of star formation to the present epoch, a stellar population that is not possible with a simpler star formation history.

This method can model a young stellar population, (like Model 3), but is unable to recover a star-burst or mixed populations (Models 8 and 2 respectively) based on SED fitting. The “old & young burst” of Model 2 is not particularly blue and as such, we identify an age of 4.4 Gyr. We do better with Model 3 where we estimate the correct age of 1.4 Gyr with a small uncertainty.

Figure 2 shows the FSPS output SEDs of the initial input star formation parameters and the best-fit parameters from our analysis. The SEDs are fit very well

<sup>5</sup> A mathematical description is available in [VanderPlas \(2014, Appendix A\)](#); he also has a nice graphical example on his [website](#).



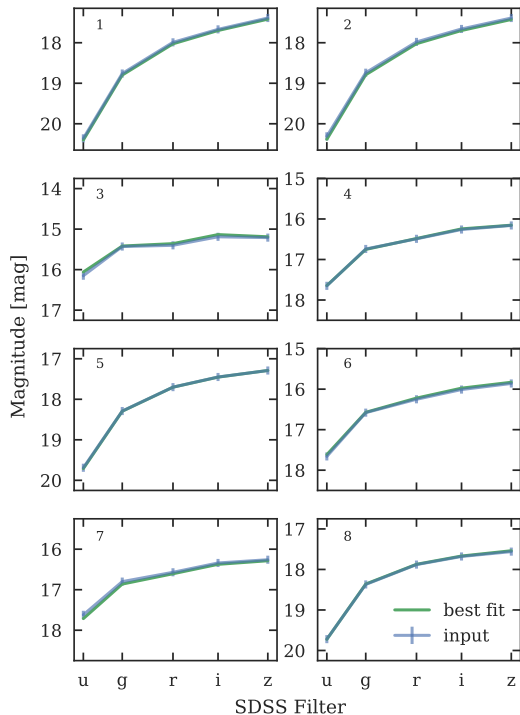


**Figure 2.** The FSPS produced SEDs (blue lines labeled inputs) from the initial parameters (available in Table 5) as well as the best fit values derived by our new Bayesian age estimator. For these eight stellar populations, covering most of our model space, the fits are excellent matches to the input SEDs.

across all the models used in this self-consistency test. In addition to fitting the SEDs, our analysis was able to approximate the underlying parameters. An example corner plot of the posterior probabilities is displayed in Figure 3, and the full set of figures is available online.

### Fig. Set 3. Self-consistency posterior results.

#### 5.2. Comparison to Previous Work

The final validation was to recalculate the global host ages originally presented in G11. A direct comparison between ages from G11 and the results from our analysis can be seen in Figure 4. Most points fit along the one-to-one line with a scatter of around 2 Gyr implying that our analysis is consistent with the previous work. However, there are six hosts that our method estimates to be  $\lesssim 2$  Gyr, whereas none of the ages in G11 were that young. At  $\lesssim 4$  Gyr, our method systematically estimates a younger age. This is because our star formation history model allows for more recent star formation

than the simple  $\tau$  models permits. In their discussion on this topic, Simha et al. (2014) claimed that the star formation model used in G11 can overestimate young populations by  $\sim 2$  Gyr. This overestimation can be seen in Figure 4.

## 6. RESULTS

Our analysis generates a probability distribution for the age of a stellar population. Probability distributions can be summarized by a median and 68% confidence intervals, especially if the distribution is Gaussian. For non-normal distributions, particularly ones with long tails or multiple modes, the distribution can still be summarized by a median age, but its interpretation is not as clear. To accurately represent the estimated age posterior probabilities shown in Figures 5, 6 and 8, we plotted the results of 100 random samples from both the age and Hubble residual distributions for each SNIa. This technique results in a probability density plot of finding a SNIa at a given age and Hubble residual.

We test for correlations between parameters with the Spearman’s rank-order correlation coefficient. This is the non-parametric version of the more common Pearson’s correlation coefficient. There are several differences between Pearson’s and Spearman’s correlations. The most important difference for our study is that the Spearman’s correlation has a high absolute value for any monotonic relationship rather than just linear relationships. This means a linear, exponential, or a single step function would all rank highly with the Spearman’s correlation, but not necessarily with the Pearson’s correlation. Since several previous host galaxy studies have seen steps in Hubble residuals (or more generally sigmoid functions) it is reasonable to use a statistical measurement that is sensitive to these non-linear correlations. See Wall & Jenkins (2012, section 4.2.3) for more information on the Spearman’s correlation.

A large absolute rank-order correlation refers to a tighter association of points, indicated by a small scatter around the correlation. Significance of a Spearman’s correlation can be described by a standard  $p$ -value, or the probability under the null hypothesis of obtaining a result equal to or more extreme than what was observed. Given a sample size and Spearman’s correlation a  $p$ -value can be calculated. If we let  $3\sigma$  be our significance limit, then for our main sample of 103 objects, the Spearman’s critical correlation value would be  $\pm 0.30$ . That is, there is a 0.2% chance of seeing a Spearman’s correlation value of  $> 0.3$  or  $< -0.3$  from our data set assuming no underlying correlation.

### 6.1. Global Environments

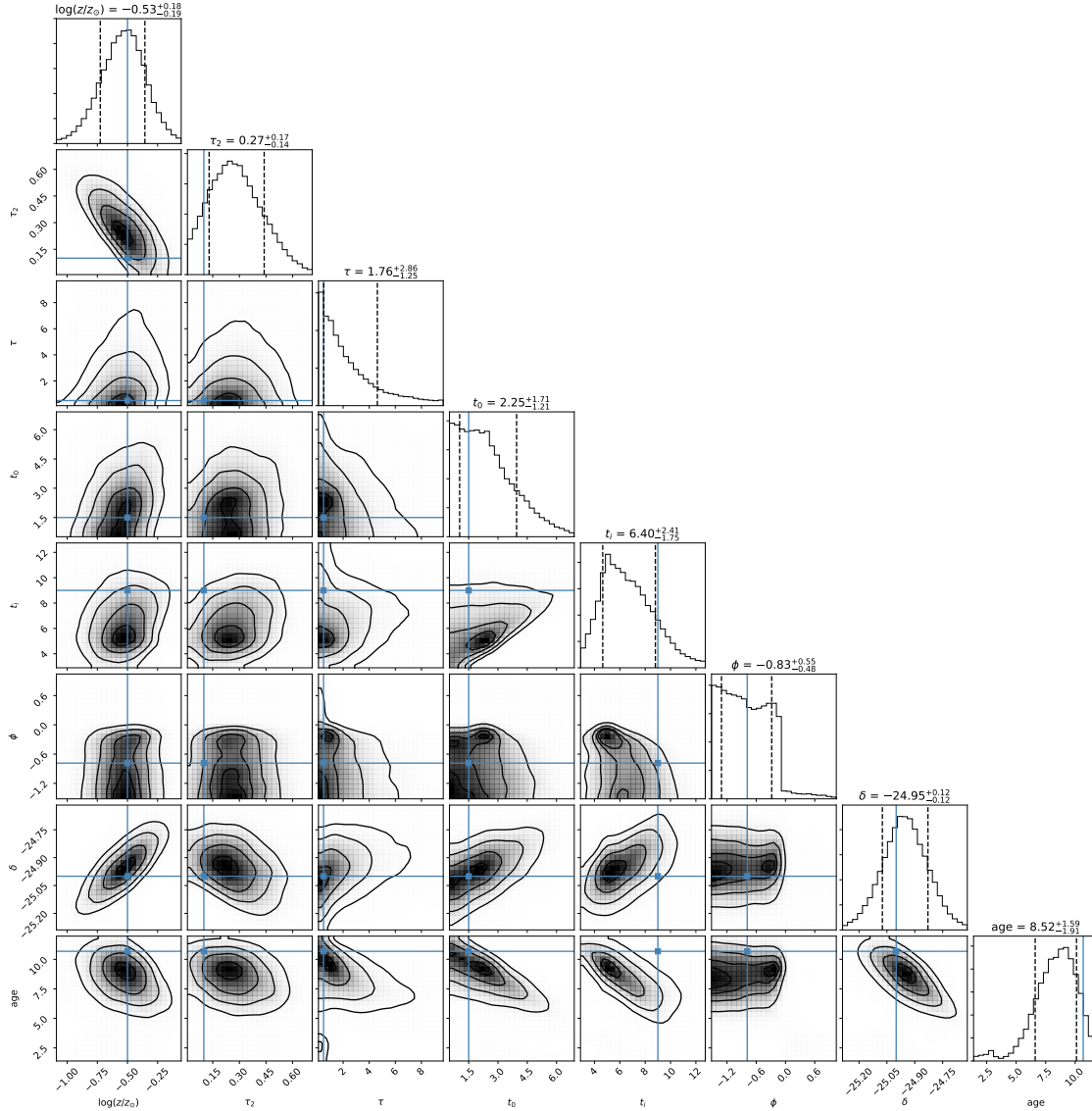


**Figure 3.** A corner plot of the posterior distribution for the first model in the self-consistency test. The input values are plotted as blue lines. The vertical dashed lines represent the 68% credible region for each parameter. The solid blue lines represent the input values as stated in Table 5. The posterior provides a good estimate of the true parameters, including the average age of the stellar population. The corresponding figure for each model (8 images) are available as a Figure Set in the online journal.

First, we compare the Hubble residuals with ages derived from the global photometry of the hosts using C13 (Table 3) sample. The comparison is presented in Figure 5. This data set has a low  $2.1\sigma$  correlation, as defined by the Spearman’s value of -0.23. In addition, the distribution in Hubble residual-age space appears to show a distinctive “step” between 7 and 8 Gyr.

### 6.2. Local Environments

Finally, we compare the Hubble residuals versus average local environment age for the data set derived from C13 (Table 1). These results are presented in Figure 6. Using an age derived from the local environ-

ment only slightly changes the Spearman’s correlation between these two parameters. But this correlation, -0.21, only has a  $1.8\sigma$  significance. The overall age distribution and apparent “step” at  $\sim 8$  Gyr are not significantly changed by switching to a local environment analysis. At first glance, the local age does not appear to contain any additional information not already present in the global age. Jones et al. (2018) found a marginally significant difference between their global and local analyses.

Because a fraction of our sample is photometrically classified, there may be some CC contamination that would be found preferentially in the upper left of Fig-

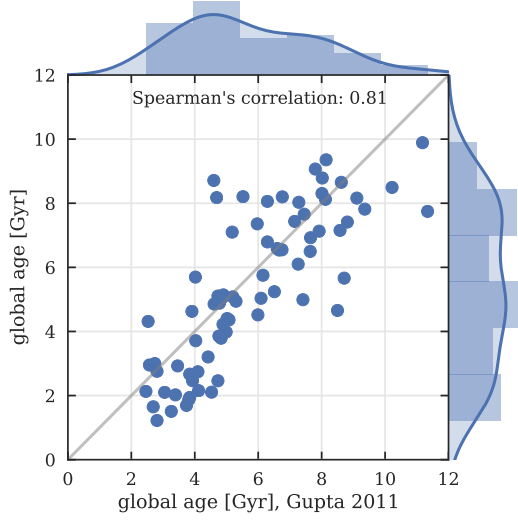


**Figure 4.** A comparison between the age estimated by the method described in this paper and the results presented in G11. They agree with a  $\sim 2$  Gyr scatter, except for the six hosts that our method estimated to be  $\lesssim 2$  Gyr but G11 estimated to be up to  $\sim 4$  Gyr. For the youngest populations ( $\lesssim 4$  Gyr), our method systematically estimates a lower age. This is expected because our method’s chosen star formation history is better at modeling young stellar populations. The  $3\sigma$  significance critical value for  $N = 76$  is a Spearman’s correlation of  $\pm 0.35$ , so it is very unlikely for this distribution, with a correlation coefficient of 0.81, to arise if these two methods were not correlated.

ures 5 and 6. This contamination might contribute to the observed correlations, but at a level that is small compared with the  $2.1\sigma$  and  $1.8\sigma$  trends.

## 7. ANALYSIS AND DISCUSSION

### 7.1. Comparison Between Local and Global Ages

The global age estimated for spiral galaxies is an average of several stellar populations. The prompt component of SNIa are expected to be found in the youngest regions of a galaxy. So we may see that the population age at the supernova location would tend to be younger than the global age of the galaxy. In Figure 7 we show the difference between the estimated global and local ages. For massive galaxies with local ages less than 4 Gyr there is a tendency for the supernova to be located in a younger than average spot in the host. The effect is less apparent for low mass galaxies, but that is likely because the size of the region measured for the local environment is a large fraction of the size of a small galaxy.

Between local ages of 4 to 8 Gyr the difference between global and local age estimates show a large scatter with no apparent trend. Beyond 8 Gyr the scatter between

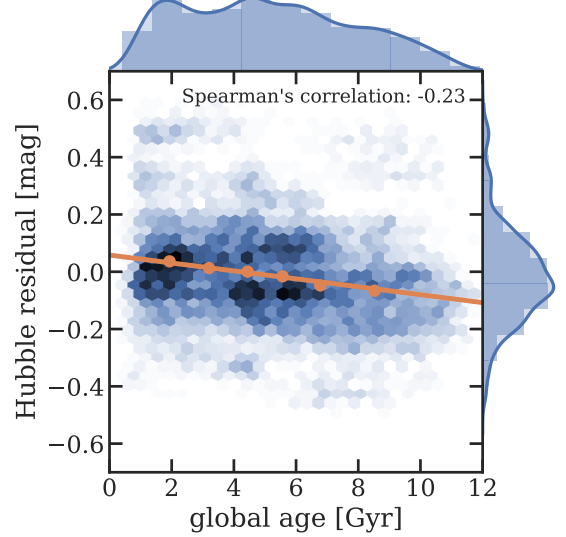


**Figure 5.** A 2D density plot (darker colors indicate a higher density) depicting the probability of finding a SNIa at a given Hubble residual and average age of its host galaxy (global age, Table 3). The presented data is a representative sampling of the underlying probability distributions for these two parameters for each SNIa in our data set. A linear fit of the data is shown as an orange line. The orange dots represent the mean of six evenly-filled bins of the underlying data. The observed correlation, with a Spearman’s correlation of -0.23, is only a  $2.1\sigma$  significance. The data shows a possible transition or “step” around 8 Gyr.

the local and global ages is reduced, probably because the stellar population in ellipticals is fairly uniform. In these older hosts the global age estimates tend to be 1 to 2 Gyr younger than the local ages. The reason for this difference is not clear, but it may be due to activity at the center of ellipticals contaminating the stellar colors.

Although we see no statistical difference between the use of local and global ages when comparing with Hubble residuals, our results suggest that using local photometry to characterize the supernova environment has some benefit over the global average. For example, the SED measured local to the supernova can indicate a population that is a factor of two younger than the global average in large star-forming galaxies. When feasible, the measurement of the local environment, particularly of younger populations, provides a more accurate representation of the progenitor age than simple averaging the light from the host.

### 7.2. Investigating the Age Step

The Hubble residuals in the C13 sample has a monotonically decreasing trend (at  $2.1\sigma$ ), that appears to be a break or step at an age of  $\sim 8$  Gyr. Figure 8 plots the same data as Figure 6 but this time splits the data

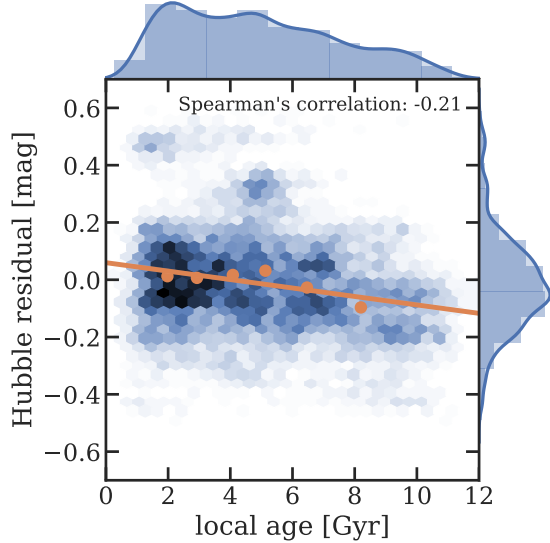


**Figure 6.** Comparing Hubble residuals of SNIa versus the average age of the local stellar environment for the sample derived from C13 (see Table 1). The data is presented the same way as Figure 5. The Spearman’s coefficient ( $-0.21$ ) is only slightly different than the one seen in Figure 5 but is insignificant only have a  $1.8\sigma$  significance. The data also has a stronger “step” at  $\sim 8$  Gyr to the global analysis. There seems to be significantly fewer SNIa with a Hubble residual at  $\gtrsim 0.0$  mag with an age  $\gtrsim 8$  Gyr.

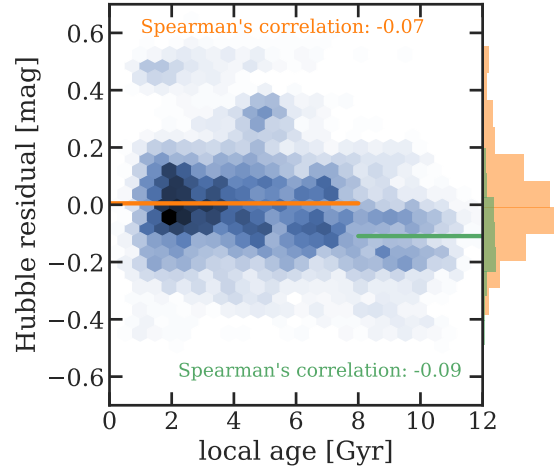


**Figure 8.** The same data as Figure 6 but with the marginalized distributions split by age. This clearly shows that the younger population ( $\leq 8$  Gyr, orange) has a higher mean Hubble residual ( $0.005 \pm 0.018$  mag) whereas the older population ( $> 8$  Gyr, green) has a lower Hubble residual mean ( $-0.109 \pm 0.035$  mag). These mean values are shown as colored lines. Due to these different means, the resulting age step is  $0.114 \pm 0.039$  mag ( $2.9\sigma$ ). The Spearman’s correlations for each piece is significantly lower than it was for the whole data set. Therefore, individually there is no meaningful trend within each subpopulation.

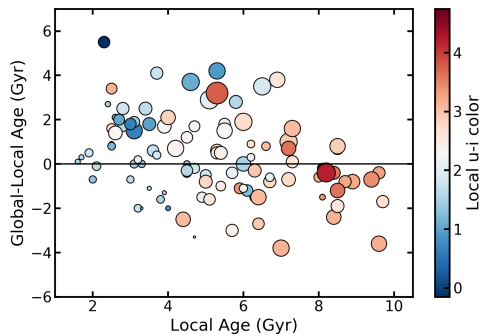


**Figure 7.** The difference in ages derived from global and local photometry as a function of local age. The size of the marker indicates the stellar mass of the host where the smallest circles show  $\log(M/M_\odot)=7.5$  and the largest circles indicates  $\log(M/M_\odot)=11.5$ . The marker color represents the  $u-i$  color index at the location of the supernova.

into two age bins:  $\leq 8$  Gyr and  $> 8$  Gyr. Both age ranges show very small Spearman’s correlations ( $-0.07$  and  $-0.09$  respectively) that are consistent with a flat distribution. The correlation decreasing in significance when the data set is split in two, implies that the monotonic function seen in Figure 6 is really a step-like function with a transition at  $\sim 8$  Gyr. This function may

have a transition width making it more like a continuous sigmoid function with a transition faster than our age resolution. In both the local and global age measurements, we find a significant age step in Hubble residuals.

The amplitude of the jump between these two populations split at  $\sim 8$  Gyr appears to be more than 0.1 mag. The younger population has a mean Hubble residual just over zero ( $0.005 \pm 0.018$  mag), whereas the older population has a mean Hubble residual of  $-0.109 \pm 0.035$  mag. This makes the resulting difference in the means equal to  $0.114 \pm 0.039$  mag ( $2.9\sigma$ ). This is almost two times larger than the commonly used mass step of 0.06 mag. A step of this size may affect precision cosmological measurements since the fraction of each subpopulation is expected to change with redshift. For example, one would not expect to find stellar populations as old as 8 Gyr at redshifts greater than  $\sim 1$  given the current standard cosmology. Such an age step may also impact local measurements of the Hubble constant as the peak luminosity of SNIa have so far been calibrated with Cepheid variables found exclusively in star forming galaxies. With the age step being detected at a  $3\sigma$  significance, Figure 8 suggests a need for an additional SNIa luminosity

correction based on their host’s local or global stellar age.

### 7.3. Age as the Cause of the Mass Step

Childress et al. (2014) argues for a link between host stellar mass and the delay time between stellar formation and SNIa explosion, with results summarized in their Figure 4 where the SNIa progenitor age distribution is divided into host galaxy stellar mass bins. They find, with reasonable assumptions of star formation histories and SNIa delay times, that there is a natural division in host mass and age between prompt and “tardy” SNIa. Prompt SNIa occur in lower mass galaxies with ages  $\lesssim 6$  Gyr while tardy events continue in high mass galaxies with ages  $\gtrsim 6$  Gyr. Projecting their model onto the host mass axis results in an overlapping distribution of prompt/tardy explosions with a transition near  $10^{10.5} M_{\odot}$ . This transition in progenitor age may correspond to the mass step observed at  $10^{10} M_{\odot}$ . Projection of the Childress et al. (2014) model onto the age axis provides a clean separation between the prompt and tardy SNIa with a dearth of events between 4 and 8 Gyr. Our age estimates are not consistent with a deficit of supernovae exploding in that range, but we do see a shift in the SNIa light curve properties around a stellar age of about 8 Gyr.

We have estimated the host galaxy masses in our sample to test if our measurements agree with the prediction of Figure 4 in Childress et al. (2014). We use the `kcorrect` code (v4.3)<sup>6</sup> described in Blanton & Roweis (2007). This code utilizes spectral fitting templates based on the stellar population synthesis models of Bruzual & Charlot (2003), which are calculated using the Chabrier (2003) initial mass function. We input the SDSS model magnitudes and the pipeline redshifts for each galaxy (presented in Table 3) to calculate the  $k$ -corrections and stellar mass-to-light ratios. The stellar masses are output in units of  $M_{\odot} h^{-1}$ , and we convert them to units of  $M_{\odot}$  using the C13 cosmology described in Section 2.4. The uncertainties on the stellar masses are approximately  $\pm 0.3$  dex. The resulting estimated stellar masses are reported in Table 7.

Figure 9 shows the distribution of the local SNIa age versus stellar mass for our sample. For our sample, the distribution of hosts in age-stellar mass space shows similarities and differences with that predicted in Childress et al. (2014). The observations do show young hosts extending to low stellar masses reproducing the backward “L” seen in the Childress et al. (2014) simulation. This

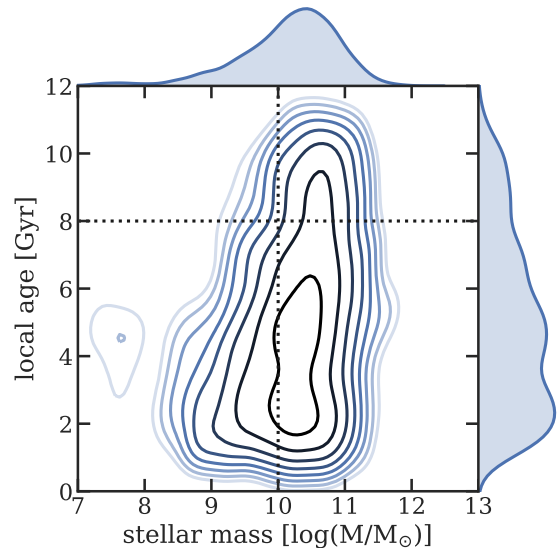


**Figure 9.** The distribution of SNIa local environment age versus host stellar mass. The two dotted lines represent the measured mass and age steps,  $10^{10} M_{\odot}$  and 8 Gyr respectively. This is in comparison to the theoretical explanation for the mass step in Childress et al. (2014). Our ages do not have as large of a range as the theoretical prediction. The expected backwards “L” shape and bi-modal features are less pronounced in our data, but not missing entirely.

indication of “cosmic downsizing” is not as pronounced in our data as we are probably still overestimating the ages of the extremely young populations. Most notably missing, is that the predicted bi-modal age feature is not present. An island of young galaxies is expected between 0.5–1.0 Gyr and that is not seen in Figure 9. Our age distribution is relatively flat from 2 Gyr to 5 Gyr and then declines out to 11 Gyr. This does not match the predicted distribution in Figure 4 of Childress et al. (2014), and there is no clear peak of old hosts. The fact that our sample of supernovae extends to a redshift of 0.2 may contribute to the lack of a clear peak in old age. Childress et al. does predict that the old-age peak decreases in height and age as the data is taken at higher redshifts simply due to the finite age of the universe.

### 7.4. Principal Component Analysis

Light curve shape and color of SNIa have been shown to be strongly correlated with peak luminosity. Other modest trends with population age, host mass, and gas metallicity have been reported and here we have identified a rather significant jump in Hubble residuals with local and global stellar age. Because these environmental observables are highly correlated with each other, it is interesting to ask if there is a linear combination of observables that have a clear and significant correlation

<sup>6</sup> Available through <http://kcorrect.org> or <http://github.com/blanton144/kcorrect>.



**Table 7.** Results of median age, stellar mass, and PC<sub>1</sub>

SN	local age	$\sigma_a$	global age	$\sigma_a$	log(M/M <sub>⊙</sub> )	PC <sub>1</sub>
762	5.1	2.7	8.0	3.9	11.1	0.07
1032	5.8	2.6	8.6	4.3	10.5	-1.78
1371	8.9	4.3	8.1	1.3	10.7	-0.82
1794	4.0	1.4	2.0	0.9	8.8	2.20
2372	5.9	1.5	4.8	2.9	10.2	-0.07

NOTE—Stellar masses have a 0.3 dex uncertainty and PC<sub>1</sub> was calculated with local environment ages. Full table is available online.

with SNIa Hubble residual. As an initial test, we performed a principal component analysis (PCA) on our data set.

PCA is a linear algebra tool that transforms the basis of a matrix of data to orthogonal axes where the new axes are maximally aligned and sorted with the intrinsic scatter of the data.<sup>7</sup> Therefore the first principal component contains the most amount of information and the last principal component contains the least. Thus, it is possible to reduce the dimensions of a problem by retaining only the principal components that comprise most of the variance (or relative information) in the original data set. In addition, the first principal component will identify a linear combination of the original variables that accounts for most of the variance in the data. Interpretation of PCA is difficult because the results are sensitive to noise, specific parameterizations, normalization, and other implementation details. However, PCA can still be useful to understand how multiple parameters work together within a data set. In the search for a trend in Hubble residuals versus SNIa parameters, we applied PCA on the parameters of SALT2 stretch ( $x_1$ ) and color ( $c$ ), as well as host mass and age. We calculated PCA coefficients first using local ages and then with global ages. Hubble residuals were not included as a PCA parameter. Only after the PCA did we search for correlations between the resulting principal components and the Hubble residuals.

Before running PCA, we normalized all parameters by removing the mean and scaling to unit variance resulting in normalized input parameters ( $x'_1$ ,  $c'$ ,  $m'$ , and  $a'$ ). An example, for  $x_1$ , is defined as:

$$x'_1 = (x_1 - \mu_{x_1})/\sigma_{x_1} \quad (10)$$

<sup>7</sup> For more information, see Ivezic et al. (2014, section 7.3), Wall & Jenkins (2012, section 4.5), or visit <https://towardsdatascience.com/pca-using-python-scikit-learn-e653f8989e60>

**Table 8.** Normalization parameters applied before PCA

	$\mu$	$\sigma$
$x_1$	-0.177	1.015
$c$	0.0100	0.0829
log(M/M <sub>⊙</sub> )	10.15 dex	0.69 dex
age	5.22 Gyr	2.11 Gyr

The means and standard deviations used in the normalization process can be seen in Table 8.

From these four observables, PCA yields four principal components (PC<sub>*i*</sub>). Table 9 shows the linear combination of the observable variables that make up each principal component as well as the explained variance. Substituting global age for local age resulted in some minor differences between the PCA coefficients and variance, but the overall conclusions are very similar between the two analyses. PC<sub>2</sub> accounts for a quarter of the variance and is dominated by the SALT2 color parameter. The other two PCA components contribute only a small portion of the variance.

As a first analysis, it is important to see if there are any correlations between Hubble residual and these SNIa-host galaxy principal components. Looking at the PCA done with local age, PC<sub>3</sub> and PC<sub>4</sub> versus Hubble residual have extremely low Spearman’s coefficients of 0.21 and −0.15 respectively. PC<sub>2</sub>, dominated by the SALT2 color term, when compared with Hubble residual is also a scatter plot with a low Spearman’s correlation of −0.06. Surprisingly there is an increase in the scatter at the high PC<sub>2</sub> (high color) domain. Using the PCA done with the global age, PC<sub>2</sub>, PC<sub>3</sub> and PC<sub>4</sub> have similar Spearman’s correlation coefficients. Figures showing the relationship between Hubble residual and each principal component (4 per analysis method, 8 total figures) are available as a Figure Set in the online journal.

#### **Fig. Set 10. Hubble residuals versus principal component**

Figure 10 shows the relationship between Hubble residuals and PC<sub>1</sub> using the estimated local age. The correlation when PCA is applied using the global host age can be seen in Figure 11 (a). PC<sub>1</sub> with either local or global ages shows a very strong correlations with Hubble residuals. The first principle component, using local age estimates, is defined as:

$$PC_1 = 0.56x'_1 - 0.10c' - 0.54m' - 0.63a' \quad (11)$$

or it can be approximated by ignoring the color term since it barely contributes to PC<sub>1</sub>.

**Table 9.** PCA coefficients using local and global ages

	$x_1$	$c$	$\log(M/M_\odot)$	age <sup>a</sup>	% variance	$x_1$	$c$	$\log(M/M_\odot)$	age <sup>b</sup>	% variance
$PC_1$	0.56	-0.10	-0.54	-0.63	44	0.45	-0.13	-0.60	-0.64	47
$PC_2$	-0.16	0.96	-0.21	-0.12	25	-0.21	0.94	-0.26	-0.10	25
$PC_3$	-0.65	-0.26	-0.71	0.07	18	-0.85	-0.32	-0.39	-0.19	19
$PC_4$	0.49	0.09	-0.40	0.77	11	-0.16	0.07	0.65	-0.74	8

NOTE—All observables are normalized via Equation (10).

<sup>a</sup>the median age of the local environment posterior

<sup>b</sup>the median global age posterior

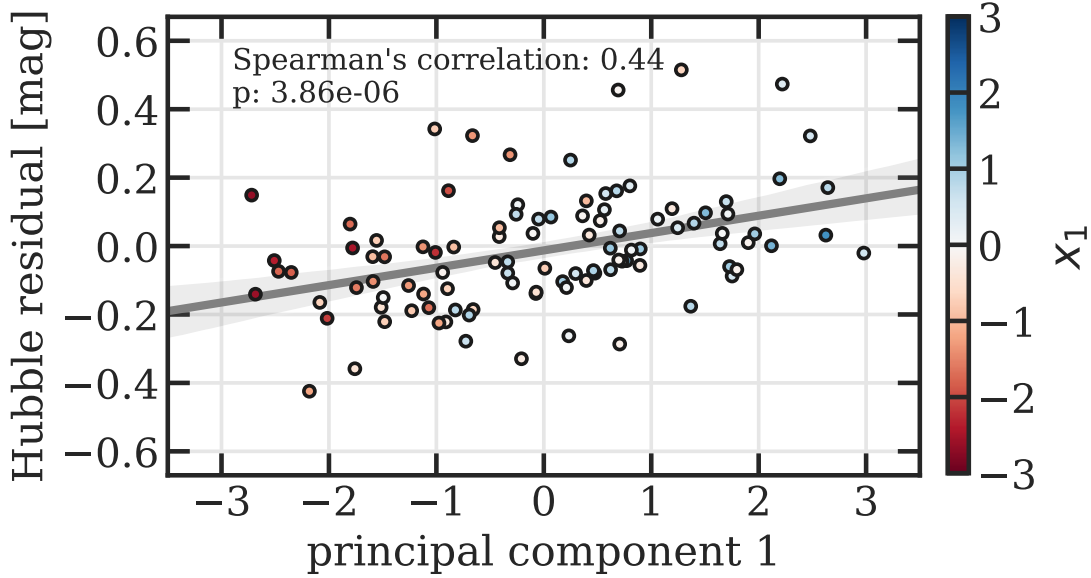


**Figure 10.** The trend between Hubble residual and principal component 1 (using local age) is clearly visible. With a Spearman's correlation coefficient of 0.44 this is a strong correlation. The p-value of  $3.86 \times 10^{-6}$  corresponds to a  $4.7\sigma$  significance. It is extremely unlikely to measure a correlation like this from uncorrelated variables. The color of each data point represents its SALT2 stretch value, red colors being a negative value and blue colors being positive values.  $PC_1$  is not simply an  $x_1$  effect because the red points are distributed across a significant range of  $PC_1$  and two blue points ( $x_1 \approx 1.5$ ) have an unexpected  $PC_1$  of  $\sim -1$ . The best fit linear regression has a slope of  $0.051 \pm 0.011$  mag and an intercept of  $-0.012 \pm 0.016$  mag. The corresponding figures for each principal component (8 total images) are available as a Figure Set in the online journal.

**Table 10.** Statistical summary of bootstrap resampling ( $N=100,000$ ) of  $PC_1$

	$x_1$	$c$	mass	age
$\mu$	0.54	-0.09	-0.52	-0.61
$\sigma$	0.08	0.17	0.11	0.06
min	-0.29	-0.95	-0.90	-0.89
max	0.85	0.93	0.31	0.06

Uncertainties for these coefficients can be obtained via bootstrap resampling (Wall & Jenkins 2012, section 6.6). Here we run a PCA on 100,000 data sets that were created randomly (with replacement) from our original data set using local ages. Since principal components are invariant to being multiplied by  $-1$ , a constraint was made that the bootstrap eigenvector needed to have a positive dot product with the original eigenvector. If this was not true, the bootstrap eigenvector's direction was reversed. The resulting distribution of coefficients for  $PC_1$  can be seen in Figure 12 and a statistical summary can be seen in Table 10. As expected, the color

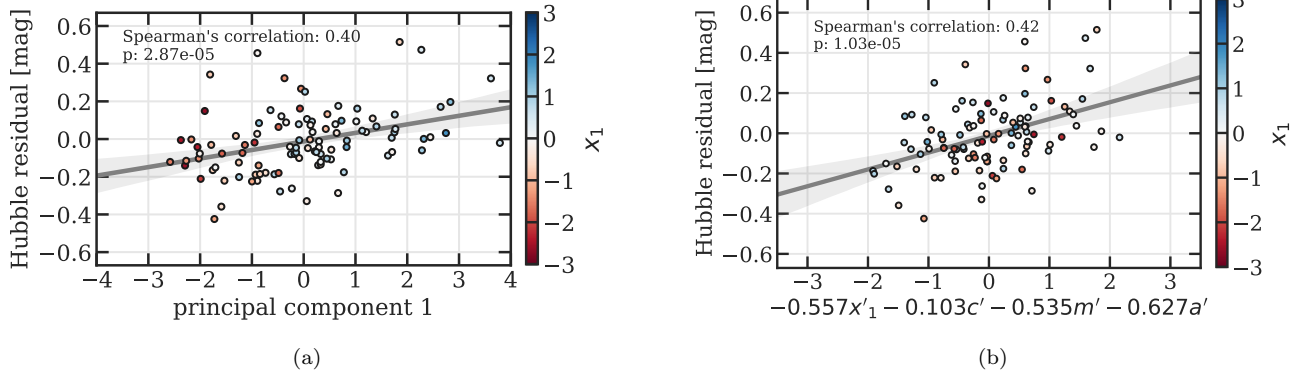


**Figure 11.** (a) Same as Figure 10, but this figure uses the PCA with global age. In this case, the correlation has a  $4.0\sigma$  significance with a linear regression with a slope of  $0.045 \pm 0.011$  mag and an intercept of  $-0.012 \pm 0.016$  mag. (b) Same as Figure 10, but calculated after reversing the sign on the  $x_1$  parameter. In this parameterization the trend with Hubble residual has a larger slope and a smaller  $\chi^2$  value than  $PC_1$ .

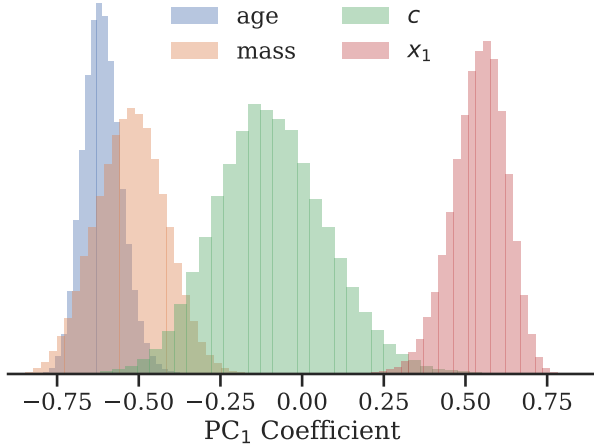


**Figure 12.** Results of a bootstrap resampling to test the robustness of the PCA, specifically  $PC_1$ . This was performed using the local age data set. It is evident that the age (blue), mass (orange), and  $x_1$  (red) coefficients are inconsistent with zero for 100,000 data sets. On the other hand, the uncertainty the coefficient for color ( $c$ , green) shows that it is consistent with zero. A statistical summary of these distributions can be found in Table 10.

coefficient is consistent with zero. Interestingly, the coefficient for local age is more constrained than for stellar mass.

In  $PC_1$ , the SALT2 color coefficient is very small, implying supernova color is not a strong contributor to this Hubble residual correlation. The mass, age, and stretch parameters in our PCA analysis are similar in amplitude and likely are of similar importance in any further standardization of SNIa distances. The SALT2 stretch parameter,  $x_1$ , has a surprising large contribution to  $PC_1$  given that the SNIa have already been corrected for light curve shape. Figure 10 suggests a correlation between

stretch and Hubble residual, but this correlation was removed at the start of the analysis. Instead,  $PC_1$  shows that the value of  $x_1$  is related to mass and age. Attempting correct for the stretch-luminosity relationship requires including host properties as all three have an influence on Hubble residuals. Our results suggest that the  $\alpha$  parameter derived from the SALT2 fit is not ideal, because the affects of host mass and population age are not distributed uniformly with stretch.

The Hubble residual- $PC_1$  correlation in Figure 10 has a Spearman's correlation of 0.44. This trend is highly significant with a p-value of  $3.86 \times 10^{-6}$  corresponding to a  $4.7\sigma$  significance. The trend in Hubble residual versus age has a significance of only  $2.1\sigma$  (Figure 5), while including mass and stretch greatly increases the significance. This strong correlation suggests that host properties influence the luminosities of SNIa beyond the currently applied corrections.

This data set did not have any significant correlations between Hubble residual and  $x_1$  or  $c$ . But, when  $x_1$  is combined with stellar mass and age there is a significant correlation with Hubble residual.

When using global ages, the underlying trend has a Spearman's correlation of 0.40 or a  $4.0\sigma$  significance. The Spearman's correlation with  $PC_1$  from local ages is slightly more significant than for global ages suggesting that measurements near the event provide some improvement in correlating supernova with environment.

The best-fit linear regression of this trend is

$$HR = 0.051 \text{ mag} \times PC_1 - 0.012 \text{ mag}, \quad (12)$$

with uncertainties in the slope and intercept as  $\pm 0.011$  mag and  $\pm 0.016$  mag respectively. This trend reduces the  $1\sigma$  scatter in Hubble residual from 0.17 mag to 0.15 mag. The best-fit linear regression using global

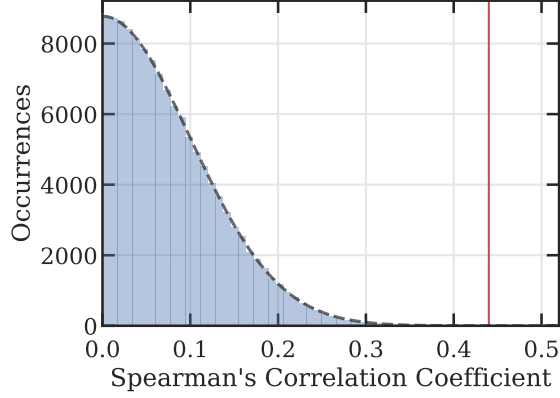


**Figure 13.** The distribution of 32,000 absolute value Spearman’s correlation coefficient for the relationship between Hubble residual and principal components of randomized SNIa  $x_1$ ,  $c$ , host mass, local environment age data sets. This distribution was generated from a bootstrap style approach that accounts for any signal PCA might produce when no underline correlation exists. With 32,000 iterations and a maximum Spearman’s correlation of 0.43, the correlation between Hubble residual and  $PC_1$  (0.44, red vertical line Figure 10) is at least  $4\sigma$  significance. This bootstrap style analysis shows that a false positive Spearman’s correlation, including any PCA effects, appears to follow a Gaussian distribution with a  $\sigma = 0.1$  (black dashed line). This is the expected distribution for Spearman’s correlation coefficients for a data set of  $N \approx 100$ .

ages values is  $HR = 0.045 \times PC_1 - 0.012$  with uncertainties in the slope and intercept as  $\pm 0.011$  mag and  $\pm 0.016$  mag respectively. This reduces the  $1\sigma$  scatter in the Hubble residual to 0.16 mag. As a note, the PCA does not maximize this correlation or minimize the  $\chi^2$  parameter in a linear regression. For example, reversing the sign of the  $x_1$  coefficient nearly doubles the slope of the correlation with Hubble residual as seen in Figure 11 (b) and significantly reduces the  $\chi^2$  parameter of a linear fit. Understanding the best use of these coefficients will be part of future work already in preparation.

Since the age and mass coefficients make up nearly two-thirds of the correlation amplitude, we see that a change of  $\pm 2\sigma$  in the normalized mass and age values results in a 0.24 mag shift in SNIa brightness. Cosmic downsizing suggests these two parameters are correlated since young galaxies tend to be small while typical old hosts are massive in the current epoch. Low-mass, young galaxies tend to be metal deficient while old, massive galaxies can be metal rich. Thus, this combination of age and mass may indicate progenitor metallicity influences the peak luminosities of SNIa.

The correlation between Hubble residual and  $PC_1$  is very significant, and it is unlikely that PCA could generate such a strong correlation from a random distribution.

To test the probability that this correlation is caused by chance, we applied a bootstrap style method for hypothesis testing. We took our PCA input matrix ( $x_1$ ,  $c$ , host mass, local environment age) and shuffled the order along each parameter, creating 103 “new” SNIa. There was no cross shuffling, so a stretch always stays a stretch, it just corresponds to a different SNIa. We applied PCA on each shuffled sample and tested for any correlations with Hubble residual. After 32,000 runs, a  $4\sigma$  test, the maximum Spearman’s correlation coefficient between Hubble residual and any principal component was 0.43 while the measured Spearman’s test of the non-shuffled values was 0.44. The distribution of the bootstrapped Spearman’s correlation coefficients is shown in Figure 13. This bootstrap style analysis shows that the false positive Spearman’s correlation follows a Gaussian distribution with a  $\sigma \approx 0.1$ . This is the expected distribution for Spearman’s correlation coefficients for a data set of  $N \approx 100$ . It is exceedingly unlikely that the correlation between Hubble residual and  $PC_1$  found in Figure 10 would appear at random. As a result, this luminosity-stretch-mass-age relationship is the most significant systematic seen between calibrated SNIa and host-galaxy environment.

#### 7.5. Correcting for the Hubble Residual- $PC_1$ Correlation

Since our  $PC_1$  strongly correlates with Hubble residuals, it is reasonable to consider a modification to the Tripp formula that is used to correct SNIa peak luminosities. The new correction coefficients would be the multiplication of the PCA coefficients and the slope of the Hubble residual- $PC_1$  trend. Except for the SALT color, the individual components making up  $PC_1$  have significant weights, so are included in this modified equation. The stretch parameter in  $PC_1$  can be grouped with the original Tripp coefficient, leaving a new term with just host properties. Since  $PC_1$  has a positive correlation with Hubble residual, the coefficient should come in with a negative sign. From these results, and following the example of others (e.g. Moreno-Raya et al. 2016b), we propose a change in the distance modulus corrections performed by SALT2 by modifying the equation to include  $PC_1$ . This new equation would be

$$\mu = m_B - M_B + (\alpha - \alpha')x_1 - \beta c + \gamma m' + \gamma a' \quad (13)$$

where  $\alpha' \approx \gamma \approx 0.03$  mag. This uses both the approximate form of  $PC_1$  and encompasses the very slight renormalization of  $x_1$  into  $x'_1$ . More research is needed to accurately determine  $\alpha'$  and  $\gamma$ .

This modified distance correction formula now includes a host galaxy stellar mass correction and a host

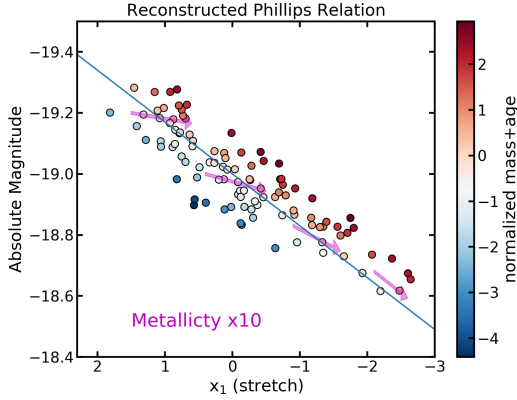


**Figure 14.** A Phillips relation reconstructed from the  $PC_1$  parameters assuming all SNIa in our sample have a peak  $M_V = -19.0$ . For the reconstruction no color correction was applied and we set the slope to the effective stretch coefficient of  $\alpha = 0.16$ . The color of the points represents the sum of the mass and age parameters. Blue points are young, low mass galaxies in our sample and red points are high mass, old hosts. The arrows approximate the predictions of Figure 4 in Kasen et al. (2009) and represent how an increase of a factor of 10 in metallicity would impact the Phillips relationship. For luminous events metallicity mainly reduces the stretch at a fixed absolute magnitude. For low-luminosity supernovae the affect of metallicity is to move the points parallel to the stretch correction correlation resulting in little impact on distance estimates.

age term. Childress et al. (2014) attempted to explain the mass step as an age dependency and we see that both appear to have an impact on SNIa luminosities. Our result is bolstered by Jones et al. (2018) who showed that stellar population color effects are still present after stellar mass corrections. Stellar mass plus population age is similar to the Mannucci relationship (Mannucci et al. 2010) that connects galaxy mass and star-formation rate with gas phase oxygen abundance. Our combined age plus mass parameters work in the same sense as the Mannucci relation and maybe a proxy for metallicity. Both Hayden et al. (2013) and Moreno-Raya et al. (2016b) have indicated that metallicity is the underlying galactic variable influencing Hubble residuals and our results support this suggestion.

Kasen et al. (2009) shows that varying the metallicity of SNIa progenitors will shift the slope of the Phillips relationship. To investigate this we assume our SNIa have a  $M_{\text{peak}} = -19$ . We then add in the Phillips relationship (with  $\alpha = 0.16$ ) and our Hubble residual- $PC_1$  relationship. The result is seen in Figure 14. Since, fast decliners are preferentially in larger and older hosts, you see the host galaxy effect on the Phillips relationship is stretch dependant. Put another way, the slope of the Phillips

relationship,  $\alpha$ , is dependant on host galaxy properties of the sample. These results show that these parameters are interrelated and that there is likely a multi-dimensional relationship between peak absolute magnitude, decline rate, and progenitor metallicity. Research into this multi-dimensional relationship will be a part of a future work already in preparation.

## 8. THE AFFECT ON $H_0$

The most precise SNIa measurement of the local value of  $H_0$  was presented in Riess et al. (2016, 2018). Riess et al. rebuilt the distance ladder connecting geometric distances, Cepheid distances and finally SNIa in the Hubble flow. These works take into account the host galaxy mass step, but this correction has a minor impact (0.7%, Riess et al. 2016) on the resulting  $H_0$ . Our trend in  $PC_1$  includes stellar age that has the potential for a significant impact on  $H_0$  since Cepheid hosts tend to have a significantly younger stellar population than the average Hubble flow galaxy. Here we put a constraint on the influence this Hubble residual- $PC_1$  trend, seen in Figure 10, may have on the measurement of  $H_0$  presented in Riess et al. (2016).

To test if the correlation in the  $PC_1$  parameter could affect  $H_0$  tension, we estimated the local age, global age and stellar mass of the SNIa hosts that have distances calibrated using Cepheid variables. We then compare the average  $PC_1$  parameter found for the Cepheid sample with the average for a Hubble flow sample. As a representative Hubble flow data set, we use our analysis of the C13 galaxies. This assumption makes our estimated shift an upper limit since the work in C13 does not include more recent corrections of small biases (e.g. Betoule et al. 2014; Kessler & Scolnic 2017) and the mass step that were performed in Riess et al. (2016). The difference in the average  $PC_1$  values for the two sets of hosts, multiplied by the slope in Equation (12) provides an estimate of the shift in peak absolute magnitude,  $\Delta M$  between the calibration sample and the Hubble flow. The fractional error in distance, and therefore  $H_0$ , due to the differences in age, mass, and stretch between the two samples is then

$$10^{\Delta M/5} - 1. \quad (14)$$

SDSS imaging was available for 14 of the 19 SNIa hosts presented in Table 1 of Riess et al. (2016). The others were outside of the SDSS footprint and without SDSS- $u$  photometry, and therefore we were not able to apply our age estimator in a consistent way. For this calibration sample, we followed the same procedures to get the local environment age, global age, and host stellar mass. These values, along with the full list of SALT2 param-



**Table 11.** Ages, stellar mass, and SALT2 values from the  $H_0$  SNIa calibration sample

SNIa	host	$x_1$	$\sigma_{x_1}$	$c$	$\sigma_c$	citation	local age	$\sigma_a$	global age	$\sigma_a$	$\log(M/M_\odot)$	$PC_{1,local}$	$PC_{1,global}$
1981B	NGC 4536	-0.32	0.14	0.030	0.010	J07	6.5	2.4	3.0	2.4	10.2	-0.49	0.61
1990N	NGC 4639	0.63	0.04	0.014	0.004	J07	6.5	1.4	4.8	3.0	10.2	0.06	0.55
1994ae	NGC 3370	0.32	0.10	-0.065	0.033	J07	5.4	1.3	5.0	1.9	10.0	0.46	0.62
1995al	NGC 3021	0.71	0.08	0.051	0.006	J07	6.4	1.7	6.0	1.5	10.2	0.06	0.16
1998aq	NGC 3982	-0.40	0.07	-0.086	0.007	J07	5.2	1.4	6.1	1.4	10.0	0.10	0.01
2002fk	NGC 1309	0.22	0.04	-0.101	0.003	S12 <sup>a</sup>	6.6	2.6	5.2	1.4	10.1	-0.06	0.44
2003du	UGC 9391	0.30	0.04	-0.100	0.004	J07	4.6	1.3	4.4	1.4	9.0	1.50	1.73
2007af	NGC 5584	-0.45	0.02	0.053	0.004	H12	6.2	1.6	6.2	2.0	9.8	-0.26	-0.13
2009ig	NGC 1015	1.76	0.15	-0.058	0.013	H12	8.8	4.4	7.9	2.1	10.3	0.01	0.20
2011by	NGC 3972	0.02	0.13	0.012	0.014	B14 <sup>a</sup>	4.5	3.0	4.1	2.6	9.8	0.60	0.78
2011fe	M 101	-0.21	0.07	-0.066	0.021	P13 <sup>b</sup>	3.1	1.0	4.9	1.2	9.9	0.88	0.46
2012cg	NGC 4424	0.45	0.04	0.080	0.020	V18 <sup>b</sup>	3.5	2.3	2.8	2.5	10.0	0.88	1.07
2012ht	NGC 3447	-1.25	0.05	-0.080	0.030	V18 <sup>b</sup>	4.0	1.3	4.4	1.4	9.2	0.63	0.79
2013dy	NGC 7250	0.70	0.04	0.089	0.025	V18 <sup>b</sup>	4.6	1.2	4.2	1.4	9.2	1.33	1.51

NOTE—Light curve parameters were estimated from cited light curves using *sncosmo* (<https://doi.org/10.5281/zenodo.592747>). Citation key: J07-Jha et al. (2007), S12-Silverman et al. (2012), H12-Hicken et al. (2012), B14-Brown et al. (2014), P13-Pereira et al. (2013), V18-Vinkó et al. (2018)

<sup>a</sup>Light curve data supplied by the Open Supernova Catalog (Guillochon et al. 2016).

<sup>b</sup>Citation is for the SALT2 parameters.

eters can be found in Table 11. A visual comparison of these parameter’s distributions can be seen in Figure 15.

The individual parameters of  $PC_1$  have only mild differences between the SNIa calibration sample and the Hubble flow hosts. The most extreme fast decliners ( $x_1 < -2$ ) are only in the Hubble flow sample because they are preferentially found in passive galaxies. The mass distributions are significantly different, with a low-mass tail in the calibration sample. The Hubble flow sample has a wider distribution of local ages than the calibration set, same with the global age. What is interesting about  $PC_1$  is that all these slight differences work in the same direction. The lower stretch, higher mass and older ages in the Hubble flow combine for a significantly lower average  $PC_1$  when compared with the larger stretch, lower mass, younger hosts from the calibration sample.

For the calibration sample, we calculated a  $PC_1$  from both the local and global age PCA methodology,  $PC_{1,local}$  and  $PC_{1,global}$  respectively. These values can also be seen in Table 11. A comparison of these two  $PC_1$  distributions are shown in Figures 16 and 17.

Using the local age, the calibration sample in Figure 16 has a mean  $PC_{1,local}$  of  $0.41 \pm 0.15$  ( $2.7\sigma$ ), while the Hubble flow  $PC_1$  mean is defined as zero. To account for the sample sizes, we performed the Kolmogorov-

Smirnov test (KS-test) resulting in a 5.5% chance ( $1.9\sigma$ ) that these samples are drawn from a common distribution and a Mann-Whitney U test indicates that the calibration sample has a higher mean at a  $1.2\sigma$  level. Using the best fit of the correlation between Hubble residual and  $PC_1$ , this corresponds to a difference of 0.021 mag.

Rerunning this analysis with the global age PCA normalization and methodology, there is a  $0.63 \pm 0.14$  ( $4.6\sigma$ ) shift in the  $PC_{1,global}$  means. The resulting KS-test says there is a 0.8% chance ( $2.7\sigma$ ) that these two samples are drawn from a common distribution. A Mann-Whitney U test indicates that the calibration sample has a higher mean at a  $2.3\sigma$  significance. Applying this shift to the trend seen in Figure 11 (a), there is a shift in peak luminosity of 0.028 mag.

These shifts in peak luminosity produces at most a 1.0% or a 1.3% effect on  $H_0$  respectively. This is about twice the size of the already accounted for mass step, but is less than the current  $1\sigma$  uncertainty in  $H_0$  (2.3%). A large SNIa systematic effect was found but it had a minimal effect on  $H_0$ . For this effect to relieve the full  $3.8\sigma$  tension (Riess et al. 2018), these two samples would need to have a  $PC_1$  shift of  $\sim 3.5$ , about 6 times larger than currently seen. The SNIa systematic found in this paper is extremely unlikely to fully resolve the  $H_0$  tension.

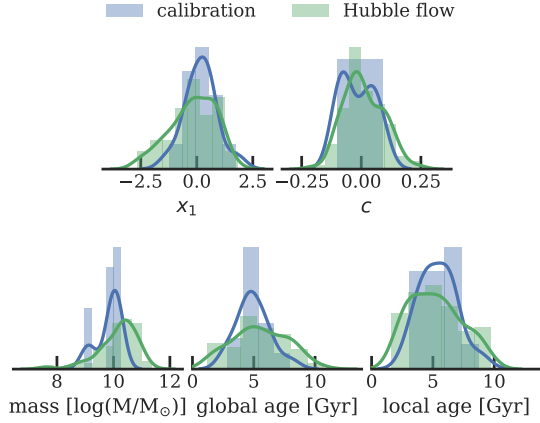


**Figure 15.** A comparison, between the local calibration SNIa sample (blue) and the Hubble flow SNIa data set (green), of the distribution of each parameter (stretch, color, host galaxy stellar mass, and average age). Histograms and kernel density estimations are shown. The Hubble flow data set has a lower  $x_1$  minimum, as expected since it has more passive galaxies. The color distributions appear to be very similar. The calibration galaxies have a lower average mass including an additional peak at  $\sim 10^9 M_\odot$  that is not seen in the Hubble flow data. This is an expected bias. The calibration age distribution is similar to, but not exactly the same as the Hubble flow sample. The main contrast is the dip in old ( $> 7$  Gyr) populations. When looking at each variable independently, only mass is drastically different, and the  $H_0$  measurement in [Riess et al. \(2016\)](#) already corrects for this effect.

## 9. CONCLUSION

Host galaxy properties have an effect on the absolute magnitude of SNIa. Host galaxy stellar mass, age, and metallicity have all been shown to be a secondary correction to the Phillips relation. Using a Bayesian method to estimate the age, we were able to look at how Hubble residuals of SNIa correlate with the mass weighted average age for both the local environment and the galaxy as a whole. This method is better at correctly estimating younger populations than previous methods. A  $2.1\sigma$  significant correlation between Hubble residual and age was seen. This correlation may be an age step of  $0.114 \pm 0.039$  mag at  $\sim 8$  Gyr. This step is nearly twice the size of the currently used mass step.

Running this analysis on both the local environment and the galaxy as a whole showed that the local age did not show any stronger of a systematic than the global age, but as expected, the local age is younger than the global age of the host for SNIa in young populations.

We are unable to completely replicate the predictions of [Childress et al. \(2014\)](#) for the distribution of SNIa hosts in the space of age versus stellar mass. The bi-

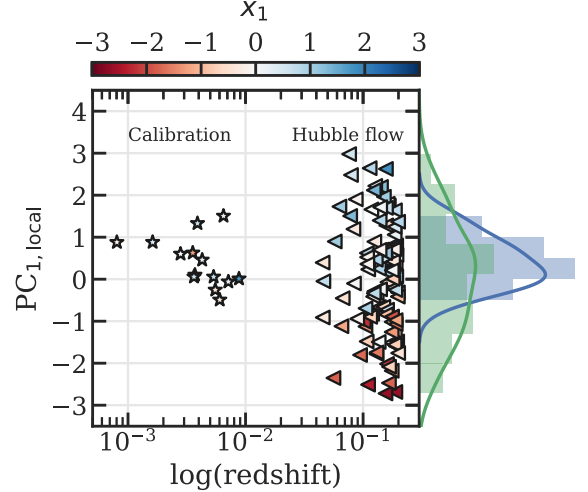


**Figure 16.** Using local age, a comparison of the two  $PC_{1,local}$  distributions for the calibration and Hubble flow SNIa samples. Histograms and kernel density estimations are shown on the vertical axis. The calibration sample has a higher mean value ( $0.407 \pm 0.15$ ,  $2.7\sigma$ ) than the Hubble flow sample (0 by definition). A KS-test concludes that these samples are different at a  $1.9\sigma$  significance. A Mann-Whitney U test says that the calibration sample has a higher mean at a  $1.2\sigma$  significance. Using the relationship between Hubble residual and  $PC_1$ , this difference would translate to a 0.021 mag shift in peak luminosity, or a 1.0% effect on  $H_0$ .

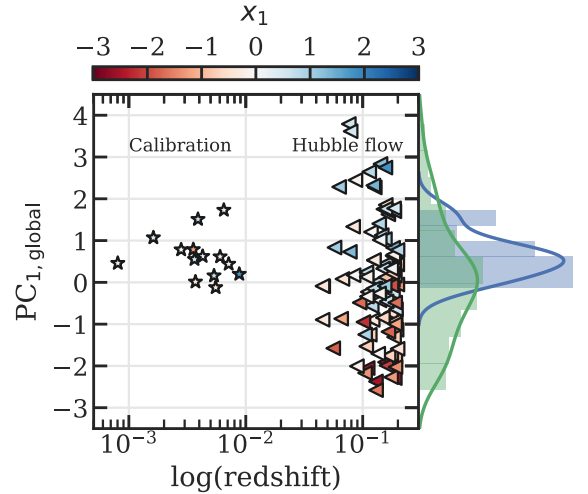


**Figure 17.** Same as Figure 16, but with global ages. Here, the calibration sample mean is  $0.63 \pm 0.14$  ( $4.6\sigma$ ). The KS-test see a difference at a  $2.7\sigma$  significance, and the Mann-Whitney U test at a  $2.3\sigma$  significance. This difference would translate to a 0.028 mag shift in peak luminosity, or a 1.3% effect on  $H_0$ .

modal SNIa age distribution is not present in the data set derived from C13, but the general trends of old galaxies with high stellar masses and a tail of low-mass young galaxies are seen in the data.

Using PCA on the two SALT2 parameters, host stellar mass, and local environment age, we see a very significant correlation (0.44) between Hubble residual and the first principal component  $PC_1 = 0.56x_1 - 0.10c - 0.54m' - 0.63a'$ . This trend was fit with a slope of  $0.051 \pm 0.011$  mag. The mixture of parameters making up  $PC_1$  suggests that to understand the luminosity variations in SNIa and to properly correct for them requires simultaneous knowledge of their host and supernova properties. This data set lacked any significant correlations between Hubble residual and  $x_1$  or  $c$ , but the combination of  $PC_1$  does have a significant correlation with Hubble residual. As a result of this significant trend,  $PC_1$  should be used as part of an updated light curve fitter.

The dominant components of  $PC_1$  are stretch, mass, and age. Using the Mannucci relationship,  $PC_1$  may be implying that  $\alpha$  has a metallicity dependence. A theoretical case for this was already made by Kasen et al. (2009), and the observational trends found in this our work are able to reproduce this predicted effect.

A correlation of this magnitude could have major effects on the precision measurement of  $H_0$ . Looking at the difference in the calibration sample and a proxy Hubble flow sample, we see that these data sets have a meaningful difference in  $PC_1$ . Using the PCA methodology and normalization from the global age analysis, there is a shift in mean  $PC_{1, \text{global}}$  of  $0.63 \pm 0.14$  ( $4.6\sigma$ ). In addition, a KS-test shows that they are drawn from different underlying populations at the  $2.7\sigma$  significance level, and a Mann-Whitney U test says the calibration sample has a higher mean at a  $2.3\sigma$  significance. Similar differences in the mean were seen using the local age. This difference between these two samples would correspond to a shift in SNIa peak absolute magnitude of 0.028 mag, or at most a 1.3% shift in  $H_0$ . This analysis only places an upper limit on this effect, because several minor bias corrections were not applied. With at most a  $\sim 0.5\sigma$  effect on  $H_0$ , this is extremely unlikely to relieve the full  $3.8\sigma$  tension between the most recent measurements of the CMB from the Planck collaboration.

A major systematic in SNIa was discovered, but it had only a small effect on  $H_0$ . This correction should be further investigated and applied to SNIa used in cosmological studies. Moreover, it appears that even a large SNIa systematic cannot fully relieve the tension between the local and CMB measurements of  $H_0$ .

The authors would like to thank Chris Wotta and Eric Bechter who provided invaluable feedback on improvements to the analysis code's design and Erika Holmbeck for suggestions on the figures. In addition, thank you to David Rubin, Daniel Foreman-Mackey, David Jones, Adam Riess, and the anonymous referee for their informative comments. Funding for this research was in part by David Eartly and the Lennox Fellowship. This research was supported in part by the Notre Dame Center for Research Computing.

Funding for the SDSS and SDSS-II has been provided by the Alfred P. Sloan Foundation, the Participating Institutions, the National Science Foundation, the U.S. Department of Energy, the National Aeronautics and Space Administration, the Japanese Monbukagakusho, the Max Planck Society, and the Higher Education Funding Council for England. The SDSS Web Site is <http://www.sdss.org/>.

The SDSS is managed by the Astrophysical Research Consortium for the Participating Institutions. The Participating Institutions are the American Museum of Natural History, Astrophysical Institute Potsdam, University of Basel, University of Cambridge, Case Western Reserve University, University of Chicago, Drexel University, Fermilab, the Institute for Advanced Study, the Japan Participation Group, Johns Hopkins University, the Joint Institute for Nuclear Astrophysics, the Kavli Institute for Particle Astrophysics and Cosmology, the Korean Scientist Group, the Chinese Academy of Sciences (LAMOST), Los Alamos National Laboratory, the Max-Planck-Institute for Astronomy (MPIA), the Max-Planck-Institute for Astrophysics (MPA), New Mexico State University, Ohio State University, University of Pittsburgh, University of Portsmouth, Princeton University, the United States Naval Observatory, and the University of Washington.

#### *Facility:* SDSS

*Software:* astropy (Astropy Collaboration 2013), astroquery (<https://doi.org/10.6084/m9.figshare.805208>), corner.py (Foreman-Mackey 2016), emcee (Foreman-Mackey et al. 2012), FSPS (Conroy et al. 2009; Conroy & Gunn 2010), kcorrect (Blanton & Roweis 2007), Matplotlib (Hunter 2007), Numpy (van der Walt et al. 2011), Pandas (McKinney 2010), Python-FSPS (Foreman-Mackey et al. 2014), scikit-learn (Pedregosa et al. 2011), SciPy (Jones et al. 2001), Seaborn (<https://doi.org/10.5281/zenodo.883859>), sfdmap (<https://doi.org/>), SIMBAD (Wenger et al. 2000), snocosmo (<https://doi.org/10.5281/zenodo.592747>)

## REFERENCES

- Arnett, W. D. 1982, *Astrophys. J.*, 253, 785
- Astropy Collaboration. 2013, *A&A*, 558, 33
- Belczynski, K., Holz, D. E., Bulik, T., & O’Shaughnessy, R. 2016, *Nature*, 534, 512
- Betoule, M., Kessler, R., Guy, J., et al. 2014, *Astron. Astrophys.*, 568, A22
- Blanton, M. R., & Roweis, S. 2007, *Astron. J.*, 133, 734
- Bravo, E., Domínguez, I., Badenes, C., Piersanti, L., & Straniero, O. 2010, *ApJ*, 711, L66
- Brown, P. J., Breeveld, A. A., Holland, S., Kuin, P., & Pritchard, T. 2014, *Astrophys. Space Sci.*, 354, 89
- Bruzual, G., & Charlot, S. 2003, *Mon. Not. R. Astron. Soc.*, 344, 1000
- Campbell, H., D’Andrea, C. B., Nichol, R. C., et al. 2013, *ApJ*, 763, 88
- Chabrier, G. 2003, *Publ. Astron. Soc. Pacific*, 115, 763
- Charlot, S., & Fall, S. M. 2000, *ApJ*, 539, 718
- Childress, M., Aldering, G., Antilogus, P., et al. 2013, *ApJ*, 770, 108
- Childress, M. J., Wolf, C., & Zahid, H. J. 2014, *MNRAS*, 445, 1898
- Choi, J., Dotter, A., Conroy, C., et al. 2016, *ApJ*, 823, 102
- Conroy, C., & Gunn, J. E. 2010, *ApJ*, 712, 833
- Conroy, C., Gunn, J. E., & White, M. 2009, *ApJ*, 699, 486
- Dotter, A. 2016, *ApJS*, 222, 8
- Falcón-Barroso, J., Sánchez-Blázquez, P., Vazdekis, A., et al. 2011, *A&A*, 532, A95
- Foley, M., Foley, R., Scolnic, D., et al. 2017, *Am. Astron. Soc. Meet. Abstr.*, 229, 341
- Foreman-Mackey, D. 2016, *J. Open Source Softw.*, 24, doi:10.21105/joss.00024
- Foreman-Mackey, D., Hogg, D. W., Lang, D., & Goodman, J. 2012, *arXiv:1202.3665*
- Foreman-Mackey, D., Sick, J., & Johnson, B. 2014, doi:10.5281/zenodo.12157
- Gallagher, J. S., Garnavich, P. M., Berlind, P., et al. 2005, *Astrophys. J.*, 634, 210
- Gallagher, J. S., Garnavich, P. M., Caldwell, N., et al. 2008, *Astrophys. J.*, 685, 752
- Garnavich, P. M., Kirshner, R. P., Challis, P., et al. 1998, *ApJ*, 493, L53
- Graur, O., Bianco, F. B., Huang, S., et al. 2016, *arXiv:1609.02921*
- Guillochon, J., Parrent, J., Kelley, L. Z., & Margutti, R. 2016, *Astrophys. Journal*, Vol. 835, Issue 1, Artic. id. 64, 15 pp. (2017)., 835, *arXiv:1605.01054*
- Gupta, R. R., D’Andrea, C. B., Sako, M., et al. 2011, *ApJ*, 740, 92
- Guy, J., Astier, P., Baumont, S., et al. 2007, *A&A*, 466, 11
- Guy, J., Sullivan, M., Conley, A., et al. 2010, *Astron. Astrophys.*, 523, A7
- Hamuy, M., Phillips, M. M., Maza, J., et al. 1995, *AJ*, 109, 1
- Hamuy, M., Phillips, M. M., Suntzeff, N. B., et al. 1996, *AJ*, 112, 2438
- Hamuy, M., Trager, S. C., Pinto, P. A., et al. 2000, *AJ*, 120, 1479
- Hayden, B. T., Gupta, R. R., Garnavich, P. M., et al. 2013, *ApJ*, 764, 191
- Hicken, M., Challis, P., Kirshner, R. P., et al. 2012, *astro-ph.C*
- Hogg, D. W., & Foreman-Mackey, D. 2017, *arXiv*, 1710.06068, *arXiv:1710.06068*
- Holtzman, J. A., Marriner, J., Kessler, R., et al. 2008, *AJ*, 136, 2306
- Howell, D. A., Sullivan, M., Brown, E. F., et al. 2009, *Astrophys. J.*, 691, 661
- Hunter, J. D. 2007, *Comput. Sci. Eng.*, 9, 90
- Ivezić, Z., Connolly, A. J., VanderPlas, J. T., & Gray, A. 2014, *Statistics, Data Mining, and Machine Learning in Astronomy* (Princeton, New Jersey: Princeton University Press)
- Jha, S., Riess, A. G., & Kirshner, R. P. 2007, *ApJ*, 659, 122
- Jones, D. O., Riess, A. G., & Scolnic, D. M. 2015, *ApJ*, 812, 31
- Jones, D. O., Riess, A. G., Scolnic, D. M., et al. 2018, *Press*, *arXiv:1805.05911*
- Jones, E., Oliphant, T., Peterson, P., & Others. 2001, *SciPy: Open Source Scientific Tools for Python*
- Kasen, D., Röpke, F. K., & Woosley, S. E. 2009, *Nature*, 460, 869
- Kasen, D., & Woosley, S. E. 2007, *Astrophys. J.*, 656, 661
- Kessler, R., & Scolnic, D. 2017, *Astrophys. J.*, 836, 56
- Lampeitl, H., Smith, M., Nichol, R. C., et al. 2010, *Astrophys. J.*, 722, 566
- Mannucci, F., Cresci, G., Maiolino, R., Marconi, A., & Gnerucci, A. 2010, *MNRAS*, 408, 2115
- McKinney, W. 2010, *Data Structures for Statistical Computing in Python*
- Moreno-Raya, M. E., López-Sánchez, Á. R., Mollá, M., et al. 2016a, *MNRAS*, 462, 1281
- Moreno-Raya, M. E., Mollá, M., López-Sánchez, Á. R., et al. 2016b, *ApJ*, 818, L19
- Pedregosa, F., Varoquaux, G., Gramfort, A., et al. 2011, *J. Mach. Learn. Res.*, 12, 2825
- Pereira, R., Thomas, R. C., Aldering, G., et al. 2013, *Astron. Astrophys.*, 554, A27

- Perlmutter, S., Aldering, G., Valle, M. D., et al. 1998, *Nature*, 391, 51
- Perlmutter, S., Aldering, G., Goldhaber, G., et al. 1999, *ApJ*, 517, 565
- Phillips, M. M. 1993, *Astrophys. J.*, 413, L105
- Phillips, M. M., Lira, P., Suntzeff, N. B., et al. 1999, *Astron. J.*, 118, 1766
- Planck Collaboration. 2016, *A&A*, 594, A13
- Planck Collaboration, P., Aghanim, N., Akrami, Y., et al. 2018, *arXiv:1807.06209*
- Riess, A. G., Press, W. H., & Kirshner, R. P. 1995, *ApJ*, 438, L17
- . 1996, *ApJ*, 473, 88
- Riess, A. G., Filippenko, A. V., Challis, P., et al. 1998, *ApJ*, 116, 1009
- Riess, A. G., Macri, L. M., Hoffmann, S. L., et al. 2016, *ApJ*, 826, 56
- Riess, A. G., Casertano, S., Yuan, W., et al. 2018, *ApJ*, 861, 126
- Rigault, M., Copin, Y., Aldering, G., et al. 2013, *A&A*, 560, A66
- Rigault, M., Aldering, G., Kowalski, M., et al. 2015, *ApJ*, 802, 20
- Rigault, M., Brinnel, V., Aldering, G., et al. 2018, *arXiv:1806.03849*
- Röpke, F. K., & Hillebrandt, W. 2004, *Astron. Astrophys.*, 420, L1
- Sako, M., Bassett, B., Becker, A., et al. 2008, *AJ*, 135, 348
- Schlafly, E. F., & Finkbeiner, D. P. 2011, *Astrophys. J.*, 737, 103
- Schlegel, D. J., Finkbeiner, D. P., & Davis, M. 1998, *Astrophys. J.*, 500, 525
- Scolnic, D. M., Jones, D. O., Rest, A., et al. 2018, *ApJ*, 859, 101
- Silverman, J. M., Foley, R. J., Filippenko, A. V., et al. 2012, *Mon. Not. R. Astron. Soc.*, 425, 1789
- Simha, V., Weinberg, D. H., Conroy, C., et al. 2014, *arXiv*, 1404.0402, *arXiv:1404.0402*
- Sullivan, M., Le Borgne, D., Pritchett, C. J., et al. 2006, *Astrophys. J.*, 648, 868
- Sullivan, M., Conley, A., Howell, D. A., et al. 2010, *Mon. Not. R. Astron. Soc.*, 406, 782
- Timmes, F. X., Brown, E. F., & Truran, J. W. 2003, *ApJ*, 590, L83
- Tripp, R., & Branch, D. 1999, *Astrophys. J.*, 525, 209
- van der Walt, S., Colbert, S. C., & Varoquaux, G. 2011, *Comput. Sci. Eng.*, 13, 22
- VanderPlas, J. 2014, *arXiv*, 1411.5018, *arXiv:1411.5018*
- Vinkó, J., Ordasi, A., Szalai, T., et al. 2018, *Publ. Astron. Soc. Pacific*, 130, 064101
- Wall, J. V., & Jenkins, C. R. 2012, *Practical Statistics for Astronomers*, second edn. (Cambridge, UK: Cambridge University Press)
- Wenger, M., Ochsenbein, F., Egret, D., et al. 2000, *Astron. Astrophys. Suppl.* v.143, p.9-22, 143, 9
- Woosley, S. E., Kasen, D., Blinnikov, S., & Sorokina, E. 2007, *ApJ*, 662, 487